New constraints on dike injection and fault slip during the 1975-84 Krafla rift crisis, NE Iceland,

J. Hollingsworth, S. Leprince, F. Ayoub, Jean-Philippe Avouac

JOURNAL OF GEOPHYSICAL RESEARCH: SOLID EARTH, VOL. 118, 3707–3727, doi:10.1002/jgrb.50223, 2013

New constraints on dike injection and fault slip during the 1975–1984 Krafla rift crisis, NE Iceland

J. Hollingsworth,[1,2] Sébastien Leprince,[1] François Ayoub,[1] and Jean-Philippe Avouac[1]

Received 31 October 2012; revised 9 April 2013; accepted 19 May 2013; published 11 July 2013.

[1] Correlation of KH9 spy and SPOT5 satellite images, airphotos, digital elevation model differencing, electronic distance measurement, and leveling survey data is used to constrain the deformation resulting from the 1975–1984 Krafla rifting crisis. We find that diking typically extends to depths of 5 km, while the dike tops range from 0 km in the caldera region to 3 km at the northern end of the rift. Extension is accommodated by diking at depth and normal faulting in the shallowest crust. In the southern section of the Krafla rift, surface opening is 80% of the dike opening at depth. Over the 70–80 km length of the rift, the average dike opening was 4.3–5.4 m. From these estimates, we calculate the total geodetic moment released over the Krafla rift crisis, $4.4–9.0 \times 10^{19}$ Nm, which is an order of magnitude higher than the seismic moment released over the same time period, $\sim 5.8 \times 10^{18}$ Nm. The total volume of magma added to the upper crust was $1.1–2.1 \times 10^{9}$ m^3. This study highlights how optical image correlation using inexpensive declassified spy satellite and airphotos, combined with simple models of crustal deformation, can provide important constraints on the deformation resulting from past earthquake and volcanic events.

Citation: Hollingsworth, J., S. Leprince, F. Ayoub, and J.-P. Avouac (2013), New constraints on dike injection and fault slip during the 1975–1984 Krafla rift crisis, NE Iceland, *J. Geophys. Res. Solid Earth*, *118*, 3707–3727, doi:10.1002/jgrb.50223.

1. Introduction

[2] Over the last 20 years, detailed geodetic observation of plate boundary zones and continental interiors has provided fundamental insight into the nature of continental deformation. In contrast, these techniques have provided relatively little information on how plates rift apart and create new crust, since these processes typically occur at oceanic spreading centers where geodetic observation is more challenging. Both normal faulting and magma injection via dikes and sills are key processes occurring within oceanic rift zones, with the interplay between these two processes playing a key role in controlling the topographic evolution of rift zones around the world [e.g., *De Chabalier and Avouac*, 1994; *Buck et al*., 2005, 2006; *Behn and Ito*, 2008; *Ito and Behn*, 2008]. However, rift zone topography is typically formed over many earthquake and volcanic cycles and thus provides only limited insight into the processes which operate over the course of a single seismic or magmatic cycle and which ultimately accommodate plate spreading.

[3] Where plate spreading occurs on land, it provides a unique opportunity to investigate both the seismic and magmatic cycles operating within rift zones using satellite geodesy [*Wright et al.*, 2012]. Unfortunately, there are few places on Earth where this occurs because plate spreading typically reduces the level of topography below that of the oceans. Furthermore, little seismic moment is released during episodic rifting events involving dike injection, thereby making them hard to detect. These factors, coupled with the narrow time window covered by satellite geodesy, mean that there are still only a few examples where dike injection and fault activation have been captured in detail.

[4] The best studied examples come from the East African rift, where major episodes of dike injection occurred in the Asal rift in 1978 [*Abdallah et al.*, 1979] and the Manda Hararo rift (Afar) in 2005–2010 [*Wright et al*., 2006, 2012]. Interferometric synthetic aperture radar measurements spanning the entire Afar crisis provided dense measurements on the surface deformation, thereby allowing the pattern of fault slip and dike opening in the upper crust to be determined through inverse elastic dislocation modeling [*Wright et al*., 2006; *Barisin et al*., 2009; *Hamling et al*., 2009, 2010; *Grandin et al*., 2010]. An important result from these studies has been the identification of a zone of reduced opening in the shallowest crust (<2 km), similar to the "shallow slip deficit" seen in various large continental strike slip earthquakes [*Simons et al.*, 2002; *Fialko et al.*, 2005; *Sudhaus and Jónsson*, 2011; *Elliott et al.*, 2012].

[5] Although the East African rift provides a setting in which dike injections can be studied using satellite geodesy,

[1]Division of GPS, California Institute of Technology, Pasadena, California, USA.
[2]Géoazur, University of Nice Sophia-Antipolis, CNRS, Observatoire de la Côte d'Azur, Valbonne, France.

Corresponding author: J. Hollingsworth, Division of GPS, California Institute of Technology, MC 100-23, Pasadena, CA 91125, USA. (james@gps.caltech.edu)

2169-9313/13/10.1002/jgrb.50223

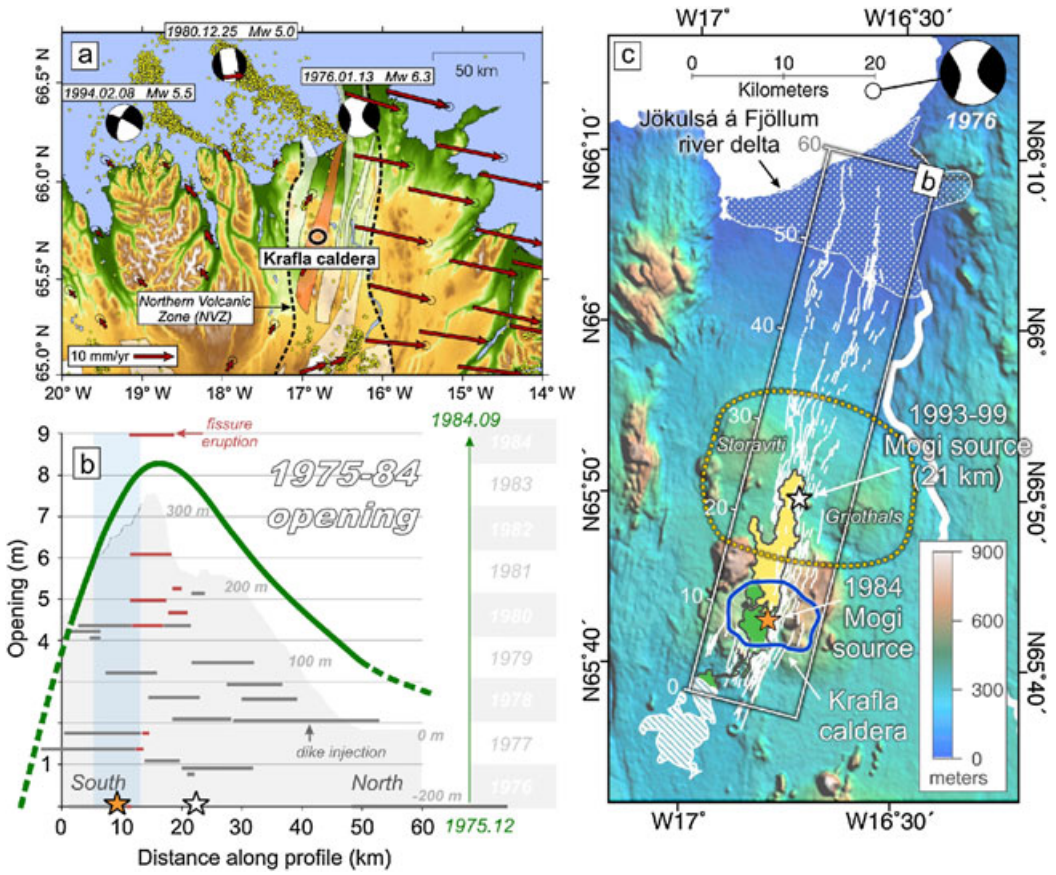

Figure 1. (a) Topographic map of the northern central region of Iceland. Yellow circles show the location of microearthquakes ($M_w \geq 2.8$) between 1990 and 2010 from the South Iceland Lowland earthquake catalog of the Iceland Meteorological Office. Red arrows show GPS velocities from *Árnadóttir et al.* [2009] relative to stable North America. Black earthquake focal mechanisms are earthquake centroid determinations from the Global centroid moment tensor (CMT) catalog. Heavy dashed black lines show the boundaries of the Northern Volcanic Zone (NVZ), across which all the plate spreading between Eurasia and North America is accommodated at this latitude. Transparent white areas highlight the various fissure swarms which lie within the NVZ, which accommodate this plate spreading through a combination of fault slip and magmatic injection. The red area highlights the Krafla fissure swarm. The heavy black circle shows the location of the Krafla caldera. (b) Profile showing the total amount of opening along the fissure swarm, based on survey data from *Tryggvason* [1984] and image correlation data from *Hollingsworth et al.* [2012], overlying a swath topographic profile along the length of the Krafla fissure swarm (corresponding to the white box in Figure 1c). Horizontal black lines show the lateral extent and timing of dikes injected into the crust throughout the crisis; red lines show fissure eruptions. Vertical blue line shows the location of the Krafla caldera. (c) Topographic map of the Krafla region. White lines indicate faults active during the Holocene. Heavy white line and stippled white region show the Jökulsá á Fjöllum river and delta. White dashed region is Myvatn lake. Blue circle shows the limits of the Krafla caldera. Orange star shows the location of the best-fitting mogi source (i.e., magma chamber) beneath the Krafla caldera, calculated from inversion of geodetic data spanning the 1984 eruption [*Árnadóttir et al.*, 1998]. White star shows the location of a much deeper magma source at 21 km, which is currently inflating [*de Zeeuw-van Dalfsen et al.*, 2004]. This also corresponds to a broad zone of uplift comprising the Storaviti and Grjothals topographic highs (yellow dotted line). The Global CMT solution is shown for the 13 January 1976 earthquake.

it is not a true oceanic rift zone and therefore may differ from plate spreading in an oceanic setting.

[6] The 1975–1984 Krafla rift crisis in NE Iceland provides a unique example where episodic dike injection was captured geodetically, albeit by traditional surveying techniques rather than satellite geodesy, in an oceanic rift setting, albeit one also under the influence of a hot spot activity (Figure 1) [*Björnsson et al.*, 1977; *Sigmundsson*, 2006]. By comparing the results from elastic dislocation models with leveling data from the northern end of the rift, *Rubin and Pollard* [1988] and *Rubin* [1992] found the surface extension to be 160% of the thickness of the dike at depth. In contrast, using a similar approach, the authors found surface extension to be only 40% of that at depth (more consistent

with deformation in the Afar crisis) for the southern end of the rift. Although these studies highlight the heterogeneous nature of deformation along strike of the Krafla rift zone, they only focus on two dike injections out of 15–20. Therefore, very little is known about the total 3-D distribution of fault slip/dike opening throughout the entire Krafla rifting crisis. The goal of this paper is to better address this problem using recent measurements from correlation of declassified optical satellite and aerial photos [*Hollingsworth et al.*, 2012], in combination with DEMs computed from aerial photos, and preexisting geodetic data. Although various data limitations prevent an inversion scheme for the slip/opening distribution as used in Afar [e.g., *Grandin et al*., 2009], we are nevertheless able to constrain the first-order pattern of crustal deformation preserved in these data sets using a simpler modeling approach similar to that used by *Rubin and Pollard* [1988] and *Rubin* [1992]. Nevertheless, we acknowledge that simple dislocation modeling using an elastic half-space [*Okada*, 1985, 1992] may not simulate well the effects of brittle deformation in the subsurface of the Krafla rift zone, where rocks are extensively fractured and subject to low confining stress, leading to a significant amount of anelastic deformation. Furthermore, the high geothermal gradient will lead to a more complicated elastic structure with depth.

2. Overview of the 1975–1984 Krafla Rifting Crisis

[7] On 20 December 1975, intense microseismicity, tilting, and eruption of volcanic material occurred in the Krafla caldera region of the Northern Volcanic Zone of NE Iceland, marking the onset of a 9 year period of seismic and volcanic activity in which the crust extended by up to $\sim$ 9 m [*Björnsson et al.*, 1977; *Tryggvason*, 1994; *Hollingsworth et al.*, 2012]. During this time, various dikes were injected into the crust, propagating 70–80 km along a NNE-striking zone of intense surface faulting and fissuring, known as the Krafla Fissure Swarm. Seismic activity remained high until January–February 1976, with much of the activity confined to the caldera itself. However, the largest earthquake of the entire crisis occurred $\sim$70 km north of the caldera on 13 January 1976 (M_w6.3). This earthquake occurred offshore in the Axarfjördur region (Figure 1c). The right-lateral focal mechanism suggested slip on a NW-SE transform fault, in response to NW-SE extension further south in response to the dike injection. However, *Hollingsworth et al.* [2012] have suggested that the dilatational component in the focal mechanism may result from a separate dike injection at the northern end of the rift.

[8] Various dikes were injected over the following years, mostly in the caldera region near the southern end of the fissure swarm. Only one further dike (January 1978) was thought to extend northward as far as the Jökulsá á Fjöllum river delta (Figures 1b and 1c). Lavas were erupted close to the caldera region, and mostly during the latter stages of the crisis, presumably once dikes had relieved all the extensional stress at depth. The crisis ended with the most extensive eruption between 4 and 18 September 1984, which covered the caldera and extended 10 km to the north (Figure 1c). Between 1975 and 1984, around nine separate eruptions occurred and 20 dikes were injected into the crust, which resulted in 9–10 m of opening near the caldera, decreasing to 3–4 m near the coastline to the north [*Wendt et al.*, 1985; *Tryggvason*, 1984; *Árnadóttir et al.*, 1998; *Buck et al.*, 2006; *Hollingsworth et al.*, 2012]. The non-uniform pattern of surface opening, which resembles triangular slip distributions for various large earthquakes [*Manighetti et al.*, 2005] therefore raises questions about how plate spreading is accommodated throughout the Northern Volcanic Zone over geological time.

3. Methodology and Data

3.1. Data (Pre-crisis and Post-crisis)

[9] In this paper, we use measurements of surface deformation obtained by the optical image correlation technique as input for both inverse and forward elastic dislocation models to better constrain the style and magnitude of deformation throughout the Krafla rift zone. This technique compares two images of the Earth's surface that were acquired at different times and estimates any pixel shifts between them with subpixel precision. This technique takes advantage of the recently developed COSI-Corr software package (COSI-Corr, available for free download from www.tectonics.caltech.edu/slip_history/spot_coseis/index.html), which allows optical images to be ortho-rectified, co-registered, and then correlated using an iterative, unbiased processor that estimates the phase plane in the Fourier domain [*Leprince et al*., 2007b, 2007a, 2008; *Ayoub et al*., 2009a]. This process produces two correlation images, each representing one of the horizontal ground displacement components in the East-West and North-South direction. In practice, this technique is able to resolve displacements as low as one tenth of the input pixel size. Images can be successfully correlated with each other, despite the wide variety of imaging systems used to acquire data. The methodology for correlating historical satellite and airphoto data differs from modern satellite data, since the images were acquired with a film-based frame camera system, rather than a pushbroom sensor (for a detailed description for correlating airphotos, see *Ayoub et al*. [2009a]). Knowledge of the camera system (such as the focal length, fiducial lengths, optical distortion) used to acquire airphotos or film-based satellite images is required to determine the interior orientation parameters of the camera, which is in turn needed to successfully ortho-rectify and co-register the images using COSI-Corr. In the case of airphotos, this information is typically available in the form of a calibration report which accompanies the images.

[10] In this study, we build on the study of *Hollingsworth et al*. [2012], who correlate KH9 spy satellite, SPOT5 satellite, and airphotos to measure surface deformation throughout the Krafla rifting crisis. For more details on the data used and how it was processed, the reader is referred to their paper. Because optical image correlation primarily constrains the horizontal displacement field, we create high-resolution digital elevation models (DEMs) from stereo airphotos of the Krafla rift zone acquired before and after the crisis. The relative difference between these DEMs reveals the vertical deformation within the rift, thereby allowing us to resolve the full 3-D deformation field for certain locations in the rift zone. Stereo DEMs are extracted using Leica Photogrammetry Suite, which is available as an add-on

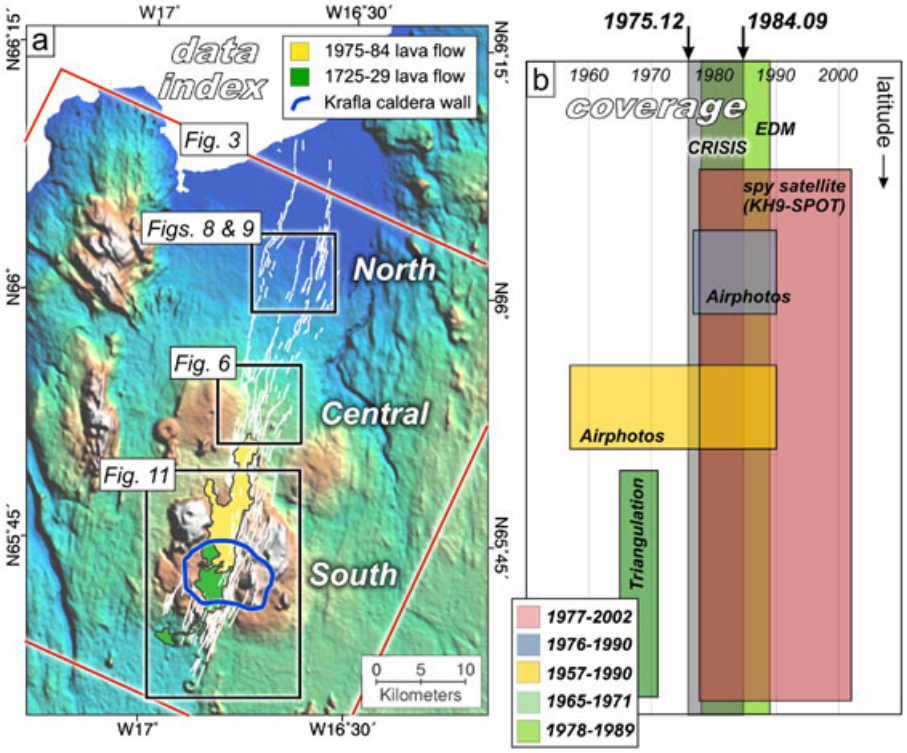

Figure 2. Topographic map of the Krafla region of NE Iceland. White lines show various faults and fissures which make up the Krafla fissure swarm and which have been active throughout the Late Quaternary. Blue circle shows the boundary of the Krafla caldera [from *Björnsson et al*., 1977], which is thought to have formed during the last interglacial (Eemian) period (114–130 kyr) [*Brandsdotttir et al*., 1997]. Yellow and green areas show the extent of lava flows during the 1975–1984 and 1725–1929 eruptions, respectively [*Björnsson et al.*, 1977]. Large red box shows the footprint of the SPOT5 satellite image correlated with a KH9 hexagon spy satellite image from 1977 (the footprint of which covers an even larger area than shown in this figure). Black boxes show the location of airphoto correlations used throughout this study. (b) Plot showing the spatial and temporal coverage of the different data sets used to constrain opening during the 1975–1984 Krafla rifting crisis. The gray zone shows the duration of the crisis.

module for the ERDAS GIS software package. This technique takes advantage of the stereo effect between different airphotos covering the same area but acquired with different view angles. The differences in parallax between two images, coupled with information on the camera system used, and ground referencing information allow the shape of the landscape to be recovered using classic photogrammetry methods [e.g., *Wolf et al*., 2000].

3.2. Inversion Methodology

[11] Using simple elastic dislocation modeling [*Okada*, 1985], we estimate the geometry and magnitude of opening/slip for dikes/faults which best fit the Krafla surface displacement field. Due to the different spatial and temporal coverage of the various optical and survey data sets used in the analysis, we focus our discussion on the southern, central, and northern ends of the rift zone separately (Figure 2). In section 4.1, we invert for the best-fitting dike and fault geometries using displacements measured from correlation of KH9 (1977) and SPOT5 (2002) images, and electronic distance measurement (EDM) data, collected between 1978 and 1989, from the southern end of the rift (Figure 4). In section 4.2, we use the horizontal displacement field from correlation of airphotos spanning the entire crisis (1957–1990), as well as vertical displacements obtained from differencing pre-crisis and post-crisis stereo airphoto DEMs (Figure 6), to constrain elastic models of diking and faulting in the central section of the rift (Figure 7). A similar approach is used in section 4.3 where airphoto (1976–1990) and KH9-SPOT5 (1977–2002) correlation data (Figure 8), DEM differencing data (1976–1990; Figure 9), and leveling survey data (1976–1978; Figure 10) are used to better constrain the 1978 dike injection in the northern end of the rift. Finally, in section 4.4, we investigate an apparent pre-crisis contraction across the rift by comparing the surface displacement field produced by deep deflation of two magma chambers (approximated by mogi sources) to triangulation data collected from the caldera region (southern end of the rift) between 1965 and 1971 (Figure 11).

[12] We use the Metropolis-Hastings algorithm (a Markov chain Monte Carlo method) [e.g., *Tarantola*, 2004; *Ofeigsson et al*., 2011; *Anderson and Segall*, 2013] to invert for the dike parameters which best reproduce the relative surface displacements close to the Krafla rift zone. This approach assumes that a dike can be described by uniform opening of a rectangular tensile crack in an elastic half-space [*Okada*, 1985, 1992], which may only be true to first order, since we are ignoring any variations in elastic structure, and

extensive fracturing of rock throughout the crust. The inversion begins with a dike model randomly generated from a range of likely dike parameter values; for each parameter, we assume a uniform probability distribution within bounds chosen a priori: (for KH9-SPOT data) depth to the top of the dike, 0.0–0.6 km; dike width, 2.0–7.0 km; opening, 3.5–8.5 m; dike length, 18.0–24 km; UTM Easting, 418000–420000—dike dip is fixed at 90°, and UTM Northing is fixed at 7297000. (for EDM data) depth to the top of the dike, 0.0–0.6 km; dike width, 2.0–7.0 km; opening, 3.5–8.5 m; dike length, 11.0–19 km; UTM Easting, 418400–420400—dike dip is fixed at 90°, and UTM Northing is fixed at 7297000. The starting range of values was estimated prior to inversion and was chosen to encompass a broad range of values which we thought would encompass the best-fitting values. We ran several test inversions, to check that our range of starting values yielded acceptance ratios of ∼50%, so the inversion would run efficiently. The only significant difference between the initial range of dike parameters in each inversion is dike length (18–24 km for KH9-SPOT and 11–19 km for EDM); these values were adjusted so the best-fitting value for dike length would fall approximately in the middle of the range of initial values. Due to the small number of EDM data points, and their limited distribution at either end of the rift, the EDM data are likely to be less accurate than the KH9-SPOT5 correlation data in constraining the dike length, which may therefore account for the difference in the best-fitting dike length values (16 km for EDM, compared with 21 km for KH9-SPOT5 data).

[13] During the inversion, the difference between the model and measured surface displacements is used to calculate the likelihood function, which is then maximized over several million iterations by use of a L2-norm cost function. This yields the most likely dike parameters describing the injection, given the range of models allowed during the inversion (equation (1)) [see also *Tarantola*, 2004].

$$L = C \times exp\left(-0.5/\sigma^2 \times \sum [M-D]^2 - log\left(\sigma \times \sqrt{2\pi}\right) \times N\right) \quad (1)$$

where L is the likelihood function, σ is the standard deviation in the displacement measurements (i.e., the error, 0.75 m for KH9-SPOT5 measurements and 0.1 m for EDM), M is the model displacement length change, D is the observed displacement length change (3-D length change for EDM data, E-W length change for the KH9-SPOT5 data), N is the number of observations made, and C is a constant used to adjust the dynamic range of the likelihood (which is forced to lie within the range 10^{15} and 10^{-15}, to avoid underflow/overflow inaccuracies when calculating the likelihood in MATLAB).

[14] Once the likelihood is computed for a given starting model, each parameter describing the dike model is randomly adjusted to create a new model and resulting likelihood value. If the "new" likelihood is greater than or equal to the "old" likelihood value, the new model parameters are accepted. Otherwise, the new model parameters are accepted based on the ratio of "old" likelihood to "new" likelihood values [for further details, see *Tarantola*, 2004]; therefore, if the model fit is only slightly worse, it is more likely to be accepted than if it is significantly worse. If a new model is rejected, the last accepted model is re-used. In this way, the model space is explored through a random walk that samples the probability density of the dike parameter space. The ability to accept a worse-fitting model means the inversion does not get stuck on local maxima in the probability density function, thereby sampling the full probability distribution. For the inversion to work efficiently, the extent to which the new model parameters can vary from the last accepted model can be adjusted so that the acceptance to rejection ratio is ∼ 50%.

4. Results

4.1. Southern Krafla Rift: Constraints on Dike Opening From KH9 and SPOT Satellite Data (1977–2002) and EDM Data (1978–1989)

[15] Figure 3a shows the results from correlating a KH9 spy satellite image from September 1977 with a SPOT5 satellite image from October 2002 [for more details, see *Hollingsworth et al*., 2012]. The displacements are projected into the rift-perpendicular direction (i.e., 104°); red values indicate eastward motion, and blue values indicate westward motion. Absolute displacements are only reliable when the pre-crisis and post-crisis images are perfectly co-registered using tie points collected from stable areas common to both images. Such areas are hard to find for Krafla because the tectonic deformation extends over a large part of the KH9 and SPOT images. Furthermore, film distortions and scanning artifacts in the KH9 image also complicate image co-registration. Therefore, a global misregistration occurs between the KH9 and SPOT5 images, resulting in E-W and N-S ramps in the displacement field. Because the eastern boundary of the SPOT5 image is probably still within the zone of deformation, subtraction of a ramp will affect the long-wavelength decay of the deformation signal which is a function of the depth extent of diking. However, short-wavelength signals are well resolved [e.g., *Ayoub et al*., 2009a], and therefore, the relative displacement gradients close to the rift zone can provide constraints on the geometry of diking and faulting throughout the crisis.

[16] To minimize outliers, the KH9-SPOT correlation was filtered with a 7 × 7 median filter, from which 75 displacement values were selected by hand (to avoid noisy areas and scan artifacts), from either side of the Krafla rift zone. Length changes between 150 randomly chosen baselines were then calculated and used as input for the inversion. This method of data selection allowed us to overcome the problem of global misregistration, which may bias the absolute displacement values, while still preserving the gradients in displacement needed to constrain the depth extent of diking. Although this approach does not account for any ramps in the data (also a result of misregistration), the ground control points (GCPs) used to co-register the KH9 and SPOT5 data come from > 20 km distance either side of the rift zone [see *Hollingsworth et al*., 2012, Figure 3] and therefore may not strongly affect the correlation data points used in the inversion, which are sampled over a narrow distance of 1–6 km either side of the rift. Furthermore, due to the fairly similar values for most likely dike depth, from inversion of the EDM data (5.5 km) and KH9-SPOT (4.2 km) using a single-dike model (Figure 4b), we assume that ramp-induced misregistrations are small. The distribution of length changes used in the inversion is shown in Figure 3b. The displacement values cover the time period September 1977 to October 2002. In

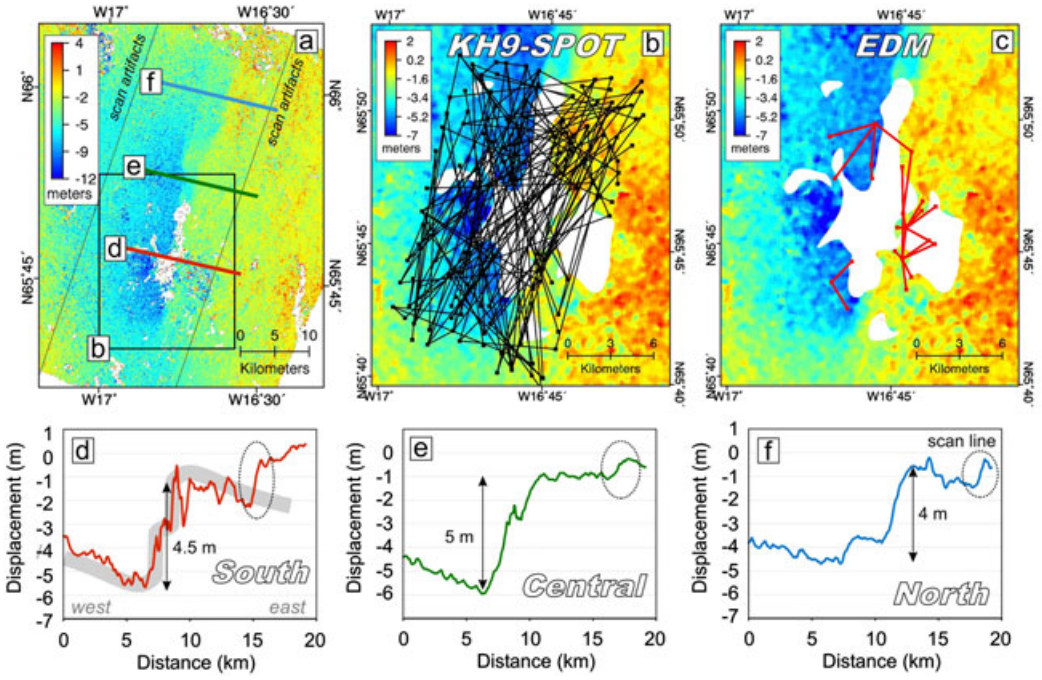

Figure 3. (a) Displacement map for the Krafla rift zone between 1977 and 2002. Displacements are perpendicular to the rift zone, which strikes 014°. Colored lines show 15 km wide swath profiles crossing the southern, central, and northern parts of the rift. (b) Displacement map corresponding to the black box in Figure 3a, showing the location of length changes (black lines) used in the inversion (we invert just the E-W component). (c) Location of length changes (red lines) measured by an EDM network (see text for details) across the southern Krafla rift. (d–f) Displacement profiles crossing the southern, central, and northern sections of the Krafla rift (see Figure 3a for profile locations). Thick gray line in Figure 3d shows the E-W displacement profile produced by the most likely dike-opening and fault slip parameters obtained by inversion; for comparison, see Figure 4. Black ellipses highlight a step in the displacement field resulting from a scanning artifact [*Hollingsworth et al.*, 2012].

addition to the image correlation data, we also invert survey measurements made from an Electronic Distance Meter network deployed between 1978 and 1989 [*Tryggvason*, 1994, Table 1]. The high precision of EDM data (< 0.1 m standard deviation compared with 0.5–1.0 m from image correlation), coupled with the similar deformation signal as recorded in the KH9-SPOT5 correlation, and coverage spanning both rift flanks (Figure 3c), allows two independent determinations of the best-fitting dike parameters. So that we can directly compare the output from both inversions, we only use image correlation displacements collected from the same region as the EDM data. To avoid complexities from shallow faulting, we only invert data from outside the rift zone, which is most sensitive to the deeper processes related to diking.

[17] Figure 4 shows the model geometry, and the resulting probability density functions for the best-fitting dike parameters (UTM Easting of the dike center, depth to the top of the dike, and the dike width, opening, and length), assuming a single-dike model, obtained by independently inverting the EDM and KH9-SPOT5 correlation data. The similarity in the best-fitting dike parameters from these two data sets, especially dike width, which is sensitive to the decay of the deformation with distance, suggests that image correlation data can be used to constrain both the surface and shallow crustal deformation (although deeper deformation may be biased by the lower signal-to-noise ratio away from the rift, and proximity of reference points used to co-register the two images). The slightly larger value of opening for the correlation data, compared with the EDM results, may result from additional diking which occurred between September 1977 and January 1978 (the time period separating acquisition of the KH9 satellite image and establishment of the EDM network; see Figure 1b).

[18] We do not attempt to invert the correlation data across the entire length of the rift zone, because a single uniform dike approximation is unlikely to be valid over the full 70 km length of the rift, and therefore unable to account for the asymmetric surface displacement field shown in Figure 1b. Furthermore, the KH9-SPOT5 data only span 80% of the crisis period, and therefore, a rift-scale inversion cannot constrain the total volume of material injected into the crust. Nevertheless, our inversion provides important constraints on the depth extent of diking (4–5.5 km) in the caldera region. Furthermore, comparing our computed values of dike opening to measurements of surface extension, we can estimate the ratio of opening between the surface and depth, which is 80% for KH9-SPOT5 data (4.75 m surface opening, Figure 3d, versus 5.9 m dike opening, Figure 4b) and 80% for EDM data (4.28 m maximum

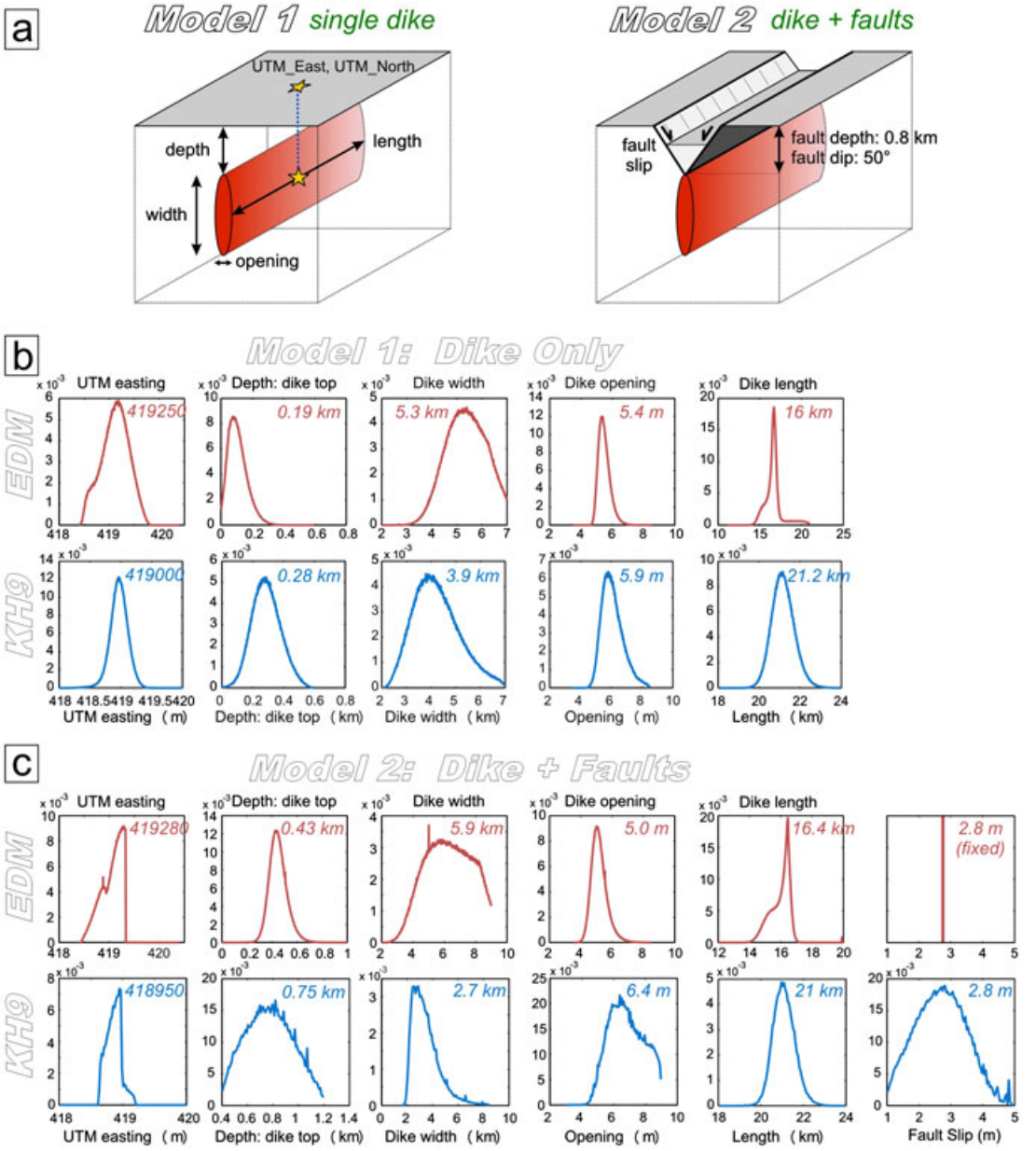

Figure 4. (a) Cartoon showing a single-dike rift model geometry (left) and dike/normal fault geometry (right), which are both inverted using a Monte Carlo inversion technique (see text for details). (b) Probability density functions for different dike parameters which best fit the EDM (1978–1989) and KH9-SPOT5 (1977–2002) correlation data, assuming a single-dike model. Each plot is made up of 15–20 separate inversions, to ensure the inversion is not sensitive to the starting model. Each inversion consists of > 3 million different models. (c) Inversion results for a dike-two fault model, although we only vary the fault slip for the KH9-SPOT correlation data inversion.

surface length change, Table 1, versus 5.4 m dike opening, Figure 4b).

[19] Because the displacement values used in our inversion lie outside the central rift zone (∼1 km wide), the best-fitting dike model is not well constrained for the shallow part of the crust (top 1 km). Also, correlation of KH9-SPOT5 and airphotos [see also *Hollingsworth et al.*, 2012] clearly reveals localized fault slip on rift-bounding normal faults, which are not accounted for by a single-dike model. Therefore, to better understand the deformation within the upper few kilometers of the Krafla rift zone, we invert both the KH9-SPOT5 correlation and EDM data using a model with two shallow normal faults above a dike (Figures 4a and 4c). The normal faults are constrained to dip at 50°, typical for oceanic normal faulting earthquakes [*Thatcher and Hill*, 1995] and consistent with predictions from rigid-plastic and elasto-plastic deformation models of normal faulting above a vertical crack [*Gerbault et al.*, 1998], and extend from the surface to a depth of 0.8 km, thus forming a 1 km wide rift valley. Using the KH9-SPOT5

Table 1. Length Changes Between Different Stations Within the EDM Triangulation Network Which Lie Outside the Rift Zone[a]

Station 1	Latitude	Longitude	Station 2	Latitude	Longitude	Length Change (m)
012	65.7185	–16.7907	006	65.7247	16.7309	0.255
012	65.7185	–16.7907	007	65.7327	16.7239	0.057
012	65.7185	–16.7907	013	65.7486	16.7497	–0.043
012	65.7185	–16.7907	019	65.7633	16.7337	–0.022
012	65.7185	–16.7907	020	65.7559	16.6981	–0.178
012	65.7185	–16.7907	021	65.7537	16.6891	–0.262
012	65.7185	–16.7907	024	65.7724	16.7391	0.005
019	65.7633	–16.7337	018	65.7636	16.7471	–0.035
019	65.7633	–16.7337	020	65.7559	16.6981	–0.172
019	65.7633	–16.7337	021	65.7537	16.6891	–0.220
019	65.7633	–16.7337	024	65.7724	16.7391	–0.013
019	65.7633	–16.7337	025	65.7746	16.7105	–0.083
019	65.7633	–16.7337	026	65.7773	16.6893	–0.222
019	65.7633	–16.7337	027	65.7804	16.7094	–0.046
035	65.8024	–16.7898	033	65.7940	16.7880	–0.103
035	65.8024	–16.7898	042	65.8284	16.7849	–0.089
042	65.8284	–16.7849	040	65.8114	16.7288	4.276
042	65.8284	–16.7849	106	65.8195	16.8546	–0.387
042	65.8284	–16.7849	108	65.7933	16.8448	–0.155
112	65.7933	–16.8448	001	65.7119	16.8207	0.625
112	65.7933	–16.8448	011	65.7413	16.8156	0.132
024	65.7724	–16.7391	037	65.8019	16.7424	0.070
024	65.7724	–16.7391	040	65.8114	16.7288	–0.017

[a]Length changes measure the displacement between 1978 and 1989 [data from *Tryggvason*, 1991]. Data points within the rift zone were not used in the inversion due to the added complexity from surface faulting. Although the 95% confidence limits for each station were given as 0.02 m in the original data table, we do not know how these were determined. Therefore, we use a higher 95% confidence limit of 0.1 m.

correlation data, we invert for the best-fitting fault slip, which is fixed to be the same for both faults, yielding values of 2.8 m. The fault slip does not converge on a best-fitting value for the EDM data, presumably due to trade-offs resulting from the sparse EDM data coverage; therefore, we fix the fault slip at 2.8 m. The inversion results for the dike and faulting model are shown in Figure 4c. The results are similar to the single-dike model, except that the depth to the top of the dike increases from 0.19 km to 0.43 km for the EDM data, and 0.28 km to 0.75 km for the KH9-SPOT5 data. The depth to the bottom of the dike increases slightly from 5.5 km to 6.3 km for the EDM data (= depth to dike top + dike width) and decreases slightly from 4.2 km to 3.45 km for the KH9-SPOT5 data. Dike opening decreases from 5.4 m to 5.0 m (EDM) and increases from 5.9 m to 6.4 m (KH9-SPOT5). Thus, inclusion of shallow normal faults does not affect the dike parameters dramatically, although the accommodation of extension by faulting in the shallowest crust tends to push the dike top to greater depths. The zone of overlap between the dike and faults is relatively small (only a few hundred meters). The ratio of surface opening to dike opening yields similar values to the single-dike model: 86% for the EDM data (4.28 m versus 5.0 m) and 74% for the KH9-SPOT5 data (4.75 m versus 6.4 m). The surface displacement profile produced by the most likely dike opening and fault slip parameters from inversion of the KH9-SPOT5 correlation data is shown in comparison with the raw KH9-SPOT5 displacement data in Figure 3d.

[20] To see how much fault slip would be expected for two stress-free planes passively slipping in response to a dike at depth, we also calculated the Coulomb stress change expected on receiver faults oriented 50° above a dike opening by 5.0 m and 6.4 m (the best-fit dike widths from EDM and KH9-SPOT5 data; Figure 5). Because we use a simple dike model with constant opening on a vertical dislocation, the Coulomb stress change goes to infinity immediately above the dike. The stress change at the surface may provide a more realistic estimate of the stress change produced by the dike; although at 0.8 km depth, the proximity to the dike tip singularity may still influence the stress changes at the surface.

[21] The Coulomb stress change at the surface produced by cumulative dike opening of 5.0 m is $\sim$ 59 MPa and 75 MPa for a 6.4 m dike. Inclusion of 2.8 m slip on conjugate normal faults above the dike relieves a large proportion of the Coulomb stress, accounting for 76% of the stress (14 MPa remaining) for a 5.0 m dike and 60% of the stress (30 MPa remaining) for a 6.4 m dike (Figures 5a and 5b). Although the residual Coulomb stress change remaining at the surface is still unrealistically high (14–30 MPa), this is strongly affected by the proximity to the singularity above the dike. Although we do not model tapering dikes in this study, to keep the modeling as simple as possible, we find that inclusion of tapered dikes significantly reduces the residual Coulomb stress at the surface to values $<$ 10 MPa. Nevertheless, to completely relieve the Coulomb stress change above the dike, we would need horizontal extension across the faults to nearly equal the dike opening, which suggests that either a deficit of slip remains in the shallow crust at Krafla or the faults had already accommodated some of this slip before the crisis began.

4.2. Central Krafla Rift: Constraints on Dike Opening and Fault Slip From Airphotos (1957–1990)

[22] Using high-resolution measurements of the horizontal and vertical deformation fields obtained from

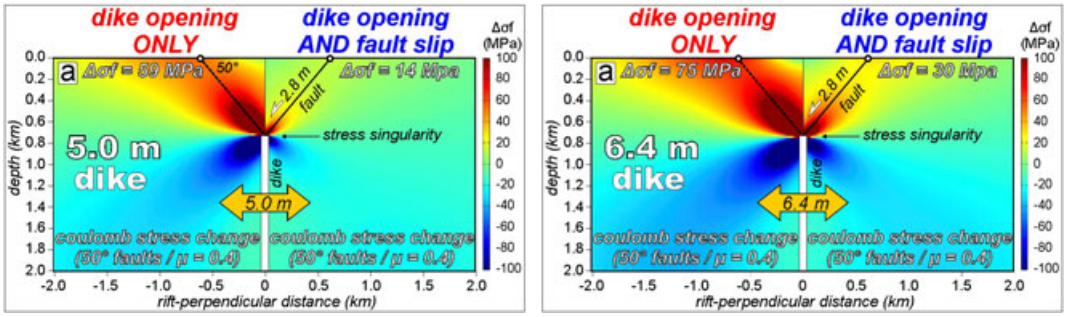

Figure 5. Cross section through the crust showing the change in Coulomb stress for 50°-dipping receiver faults above a dike opening by (a) 5.0 m and (b) 6.4 m, corresponding to the most likely dike widths found by inversion of EDM and KH9-SPOT5 correlation data. The left half of each image shows the Coulomb stress change for a dike-only model; the right side shows the stress change for a dike-fault model, with 2.8 m of fault slip (the most likely fault slip determined in our inversion). Inclusion of fault slip above the dike helps to accommodate the change in stress produced by the dike injection (see text for details).

correlation of pre-crisis (1957) and post-crisis (1990) airphotos [*Hollingsworth et al.*, 2012], and differencing of stereo DEMs extracted from the same photos (Figure 6), we run forward elastic dislocation models to further explore the geometry of faulting and diking within the central Krafla rift zone. Because the airphoto footprint is only 7–8 km wide, we are no longer sensitive to the longer wavelength deformation needed to constrain the depth of diking. However, we are sensitive to the depth of the dike top and the depth extent of normal faulting.

[23] We do not invert for the best-fitting dike and fault slip parameters, due both to the fairly complex model setting, which makes it difficult to fully explore the many trade-offs that arise from changes in geometry, and limited data coverage and quality. However, through forward modeling, we are able to show the effect of varying the depth to the dike top on the horizontal and vertical displacement field.

[24] Figures 6a and 6b show stereo DEMs for the central Krafla rift zone from 1957 and 1990 (see Figure 2 for

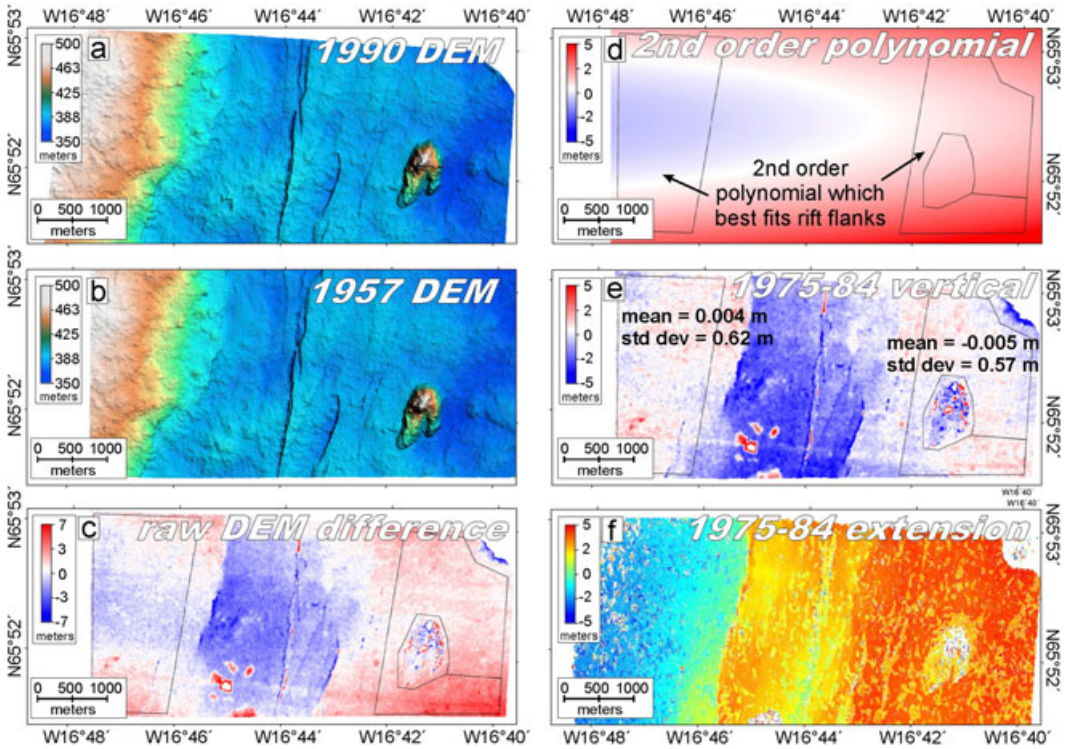

Figure 6. Stereo DEM extracted from (a) 1990 and (b) 1957 airphotos covering the central Krafla rift. (c) Vertical displacement map calculated by subtracting the 1957 DEM from the 1990 DEM. (d) Best-fitting second-order polynomial which fits the two rift flanks. (e) Vertical displacement map after removal of the second-order polynomial in Figure 6d. (f) Rift-perpendicular horizontal displacement map covering the central rift section [see *Hollingsworth et al.*, 2012].

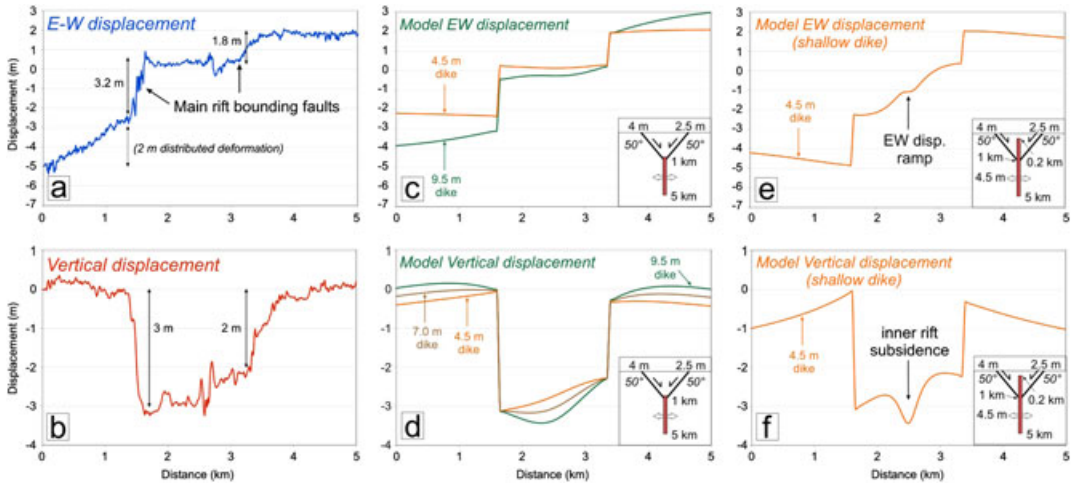

Figure 7. (a) Horizontal and (b) vertical displacement profiles spanning the central Krafla rift. Elastic dislocation models showing the (c) horizontal and (d) vertical displacements which best reproduce the observed displacement field. In these models, there is minimal overlap between diking and faulting at depth. If dikes extend closer to the surface, they would produce (e) a horizontal ramp across the rift zone and (f) a subsidence signal within the rift zone, which are both inconsistent with the observed displacements.

location). The georeferencing information for the 1990 DEM came from the 2002 ortho-rectified SPOT5 satellite image used to correlate the KH9 image; ground control points (GCPs) were collected from the rift flanks between the SPOT5 image and the 1990 airphotos. Georeferencing information from the 1957 DEM came from GCPs collected in the rift flank areas between the 1957 airphotos and the 1990 ortho-rectified airphotos. Because the rift flanks experienced vertical motions throughout the crisis, DEM differencing can only reveal relative vertical displacements. Figure 6d shows the result of subtracting the 1957 DEM from the 1990 DEM. Because the rift flank values deviate from zero, we subtract a second-order polynomial which best fits the rift flank areas (Figure 6e) to produce a map of the vertical displacement relative to the rift flanks (Figure 6f). The mean value of the rift flank areas is 0 m with a standard deviation of 0.6 m.

[25] Figures 7a and 7b show the rift-perpendicular opening and relative vertical displacement values for swath profiles across the rift (the swath size corresponds to the areas shown in Figures 6e and 6f). About 2 m extension occurs on the eastern rift boundary fault, and 5.2 m occurs on the western boundary (of which 3.2 appears to be localized onto a single normal fault and $\sim$ 2 m occurs as distributed extension over a 1 km zone to the west)—although it is difficult to assign formal errors on these estimates, inspection of the data, and comparison with different DEM outputs from Leica Photogrammetry Suite, suggests they are good within a few tens of centimeters. We run forward elastic dislocation models for two shallow normal faults (50°), which extend from the surface to 1 km depth, below which a vertical dike extends down to 5 km (consistent with the results from the KH9-SPOT5 and EDM inversions in section 4.1). We run these models for a range of dike opening values between 4.5 and 9.5 m (Figures 7c and 7d), although the small footprint of the airphotos prevents us from constraining the total dike opening. Nevertheless, these simple models reproduce well the horizontal and vertical deformations. For comparison, we also run forward models for a similar geometry of faulting and diking, except extending the dike closer to the surface (0.2 km, consistent with the EDM single-dike model in Figure 4). These models highlight the effect of extending a dike into the zone of normal faulting. In the horizontal displacement profile (Figure 7e), shallow diking produces a ramp in the horizontal displacement across the inner rift, which is not consistent with the airphoto correlation data (Figure 7a). Similarly, in the vertical displacement profile (Figure 7f), shallow diking produces a narrow zone of subsidence across the inner rift, which is not consistent with the DEM differencing data (Figure 7b). Therefore, extension in the central Krafla rift is most likely partitioned onto normal faults at the surface and dikes at depth, with relatively little overlap between the base of the normal faults and the top of the dike.

4.3. Northern Krafla Rift: Constraints on Dike Opening and Fault Slip From Airphotos (1976–1990) and Leveling Data (1976–1978)

[26] Using a similar approach to section 4.2, we compare a range of elastic dislocation models with KH9-SPOT5 and airphoto correlations (from 1977–2002 and 1976–1990, respectively), differencing of 1976 and 1990 stereo DEMs, and a leveling line survey (1976–1978), which all span the northern Krafla rift zone (Figure 2) and bracket the January 1978 dike injection (Figure 1b) [see also *Rubin and Pollard*, 1988; *Buck et al*., 2006].

[27] Figure 8a shows the KH9-SPOT5 and airphoto correlation data for the northern section of the Krafla rift, along with the locations of the leveling survey points (green circles). Extension across the rift determined from the KH9-SPOT5 correlation data is accommodated across two normal faults slipping 1.5 m and 2.6 m, respectively (from a profile 2 km south of the leveling line; Figure 8b). The correlation data also show extension beginning to die out northward,

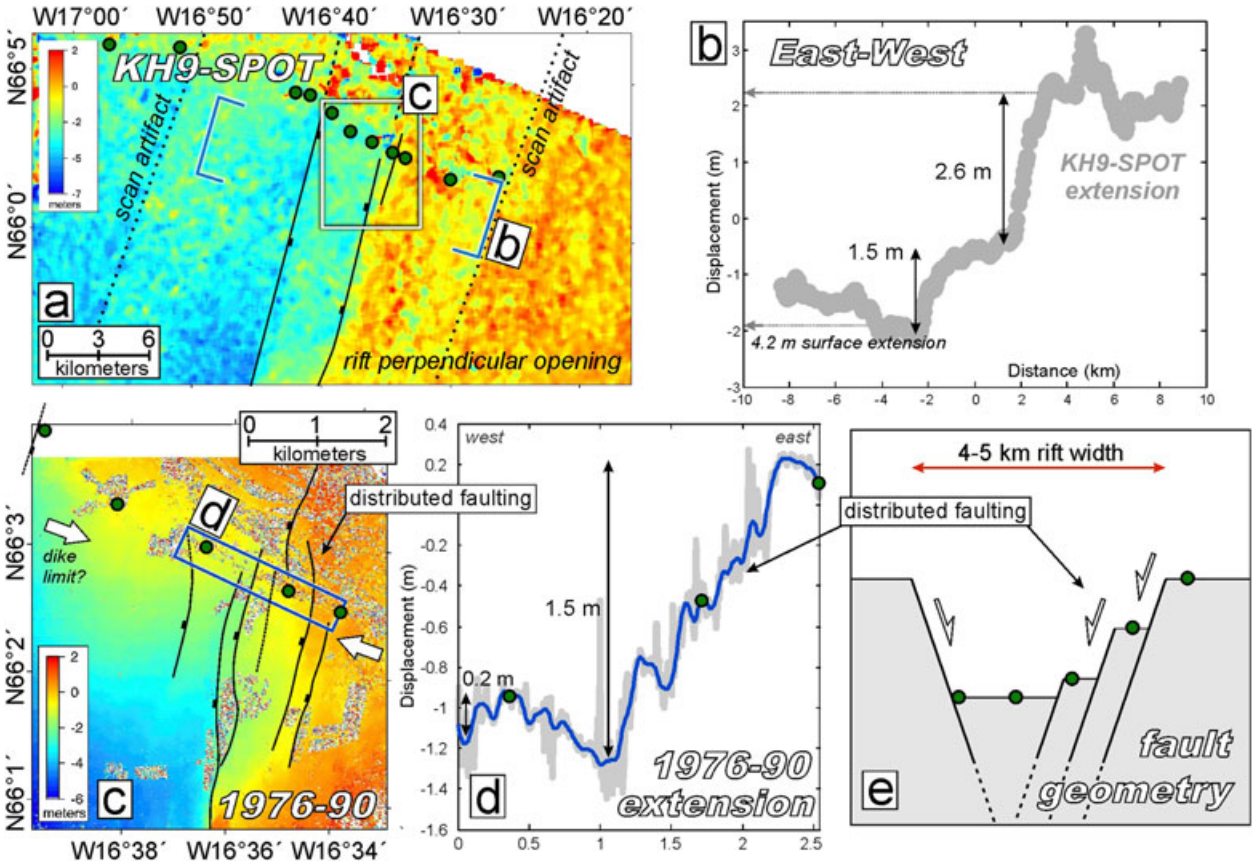

Figure 8. (a) KH9-SPOT5 correlation data for the northern section of the Krafla rift between 1977 and 2002. During this time period, the only dike injection known to have affected this section of the rift occurred in January 1978. Faults are shown schematically in black. Dotted black lines show steps in the displacement field produced by scanning the original photos. Green circles show the locations of leveling data spanning the rift. (b) Swath profile showing the displacement across the northern Krafla rift. (c) 1976–1990 airphoto correlation showing the location of leveling points within the rift. Faulting is shown by black lines. (d) Swath profile showing displacement across the east rift boundary. (e) Cartoon showing the updated fault geometry we use in our elastic dislocation modeling of the 1978 dike injection.

around the location of the leveling line. More detail on this area is provided by correlation of two aerial photos from 1976 and 1990 (Figure 8c), which also show the extension dying out around the location of the leveling line. Where the leveling data crosses the eastern margin of the rift zone, deformation is distributed across several different normal faults (Figures 8c and 8d, yielding smaller values of extension, 1.5–1.7 m). To account for this in our elastic dislocation modeling, we use the fault geometry shown in Figure 8e, which distributes the slip across several different normal faults. The geometry of diking and faulting for this section of the rift zone has previously been investigated using similar elastic dislocation models [*Rubin and Pollard*, 1988; *Rubin*, 1992]; although without the benefit of the image correlation data, these studies used just a single fault to form the eastern rift boundary.

[28] Figures 9a and 9b show the E-W extension and relative vertical deformation across the northern section of the rift, determined using the same methodology as in section 4.2. Figures 9c and 9d show swath profiles across these displacement maps (location shown by white boxes in Figures 9a and 9b) located south of the distributed rift boundary. At this location, about 2.5 m extension (Figure 9c) and 3.5 m vertical displacement (Figure 9d) are accommodated across a single fault. To help reduce long- and short-wavelength noise in the DEM differencing results, we applied a nonlocal means filter [*Buades et al.*, 2006; *Goossens et al.*, 2008; *Ayoub et al.*, 2009b] and removed a linear ramp from the displacement, so that the eastern and western boundaries of the displacement map average zero along their N-S dimension. Remaining error is difficult to quantify, although relative displacement are likely to be within 0.5 m. The E-W displacement data are better constrained and likely to have errors of a few tens of centimeters.

[29] If the decrease in E-W extension, near where the leveling line crosses the rift (Figure 9a), is due to the dike tapering out at depth, any constraints on the dike opening and fault slip determined from elastic modeling of the leveling data and/or aerial correlation data may not provide a representative estimate of the maximum dike opening and fault slip associated with the 1978 dike. Without dense and high-quality geodetic data spanning the entire rift zone south of the leveling line, we cannot well-constrain the best-fitting dike-fault slip model for the 1978 dike injection. However, we can fit relatively well the horizontal (2.5 m)

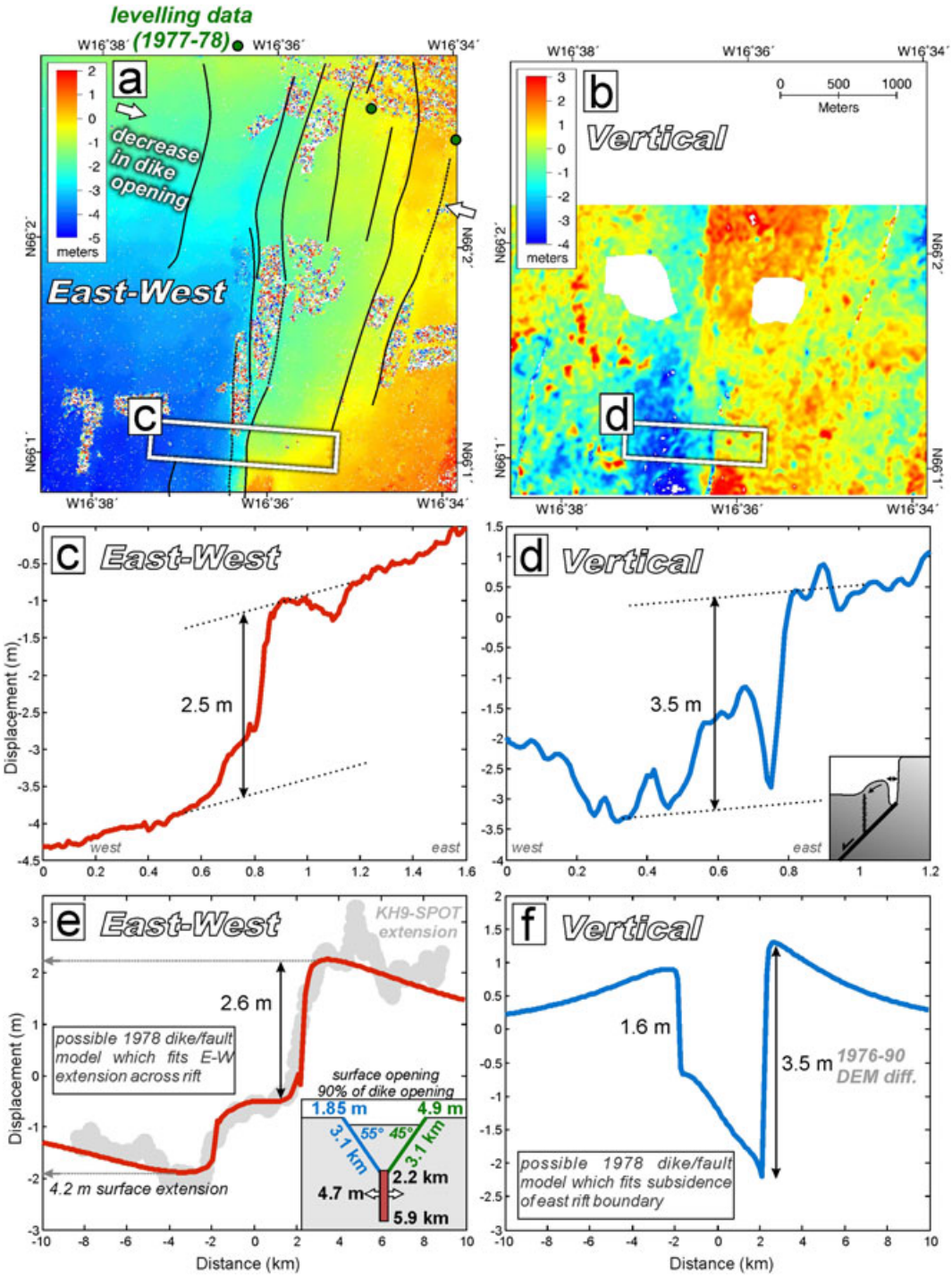

Figure 9. (a) The 1976–1990 airphoto correlation showing the location of leveling points (green circles) at eastern boundary of the rift. Faulting is shown by black lines. White arrows show the approximate location at which the E-W extension begins to noticeably die out, possibly indicating the northern dike tip. (b) Vertical displacement data from differencing of a 1976 and 1990 stereo DEM, extracted from aerial photos. (c) Rift-perpendicular (∼E-W) and (d) vertical swath displacement profile across the eastern rift boundary (see white boxes in Figures 9a and 9b for location of swath). Inset figure in Figure 9d shows a schematic cross section through crust, where a normal fault fails in horizontal tension at the surface [adapted from *Pinzuti et al*., 2010], thereby producing a surface displacement profile similar to that measured on the DEM differencing profile. (e) East-West displacement profile (red) produced by the elastic dislocation model shown in the inset. The displacement matches both the KH9-SPOT5 horizontal displacement data (2.6 m, thick gray line) and the horizontal displacement from correlation of 1976–1990 aerial photos (∼ 2.5 m), and (f) the relative vertical displacement (∼ 3.5 m) measured by DEM differencing on the eastern rift boundary.

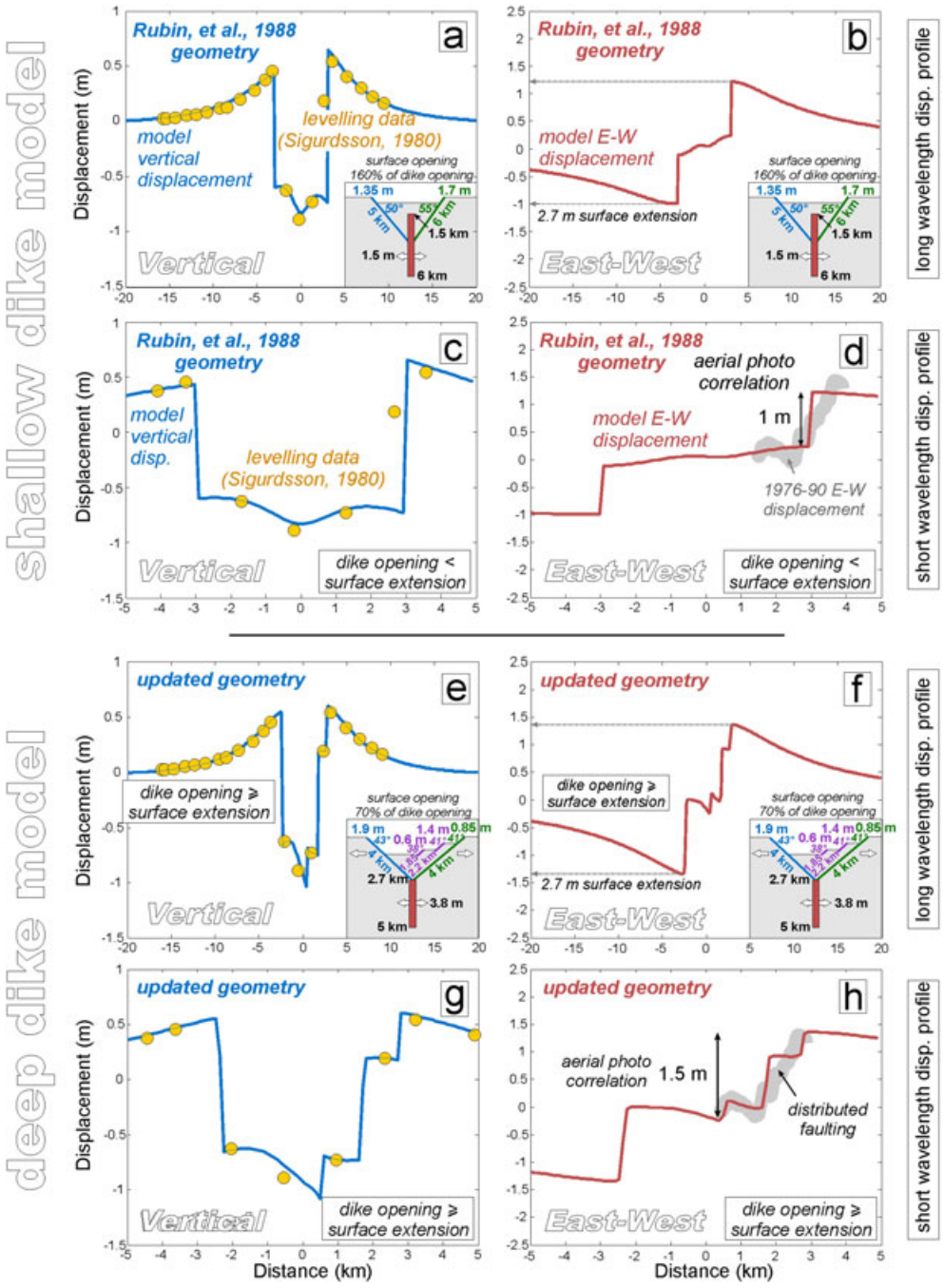

Figure 10. (a, c) Vertical and (b, d) horizontal displacement profiles over 40 km and 10 km length scales resulting from the 1978 dike injection in the northern Krafla rift. Orange circles in Figures 10a and 10c show leveling displacements [digitized from *Sigurdsson*, 1980]. Gray values in Figure 10d show extensional displacements measured from correlation of 1976–1990 aerial photos (Figure 8d). Red and blue lines show the surface displacements from the best-fitting dike-faulting model of *Rubin and Pollard* [1988] and *Rubin* [1992], shown in the inset figures. (e, g) Vertical and (f, h) horizontal displacements calculated using an updated dike-fault geometry (see inset figures), which fit both the leveling data and 1976–1990 E-W displacement data.

and vertical displacements (3.5 m) on the eastern margin of the rift, and the total horizontal extension across the rift from the lower quality KH9-SPOT data using a 4.7 m dike extending between 2.2 and 5.9 km depth, with two normal faults above slipping 1.85 m (west) and 4.9 m (east); see Figures 9e and 9f. Although this model is not well constrained, the ratio of surface extension to dike opening (90%) is more consistent with estimates from the southern Krafla rift (section 4.1) and therefore represents one of several plausible dike-fault geometries.

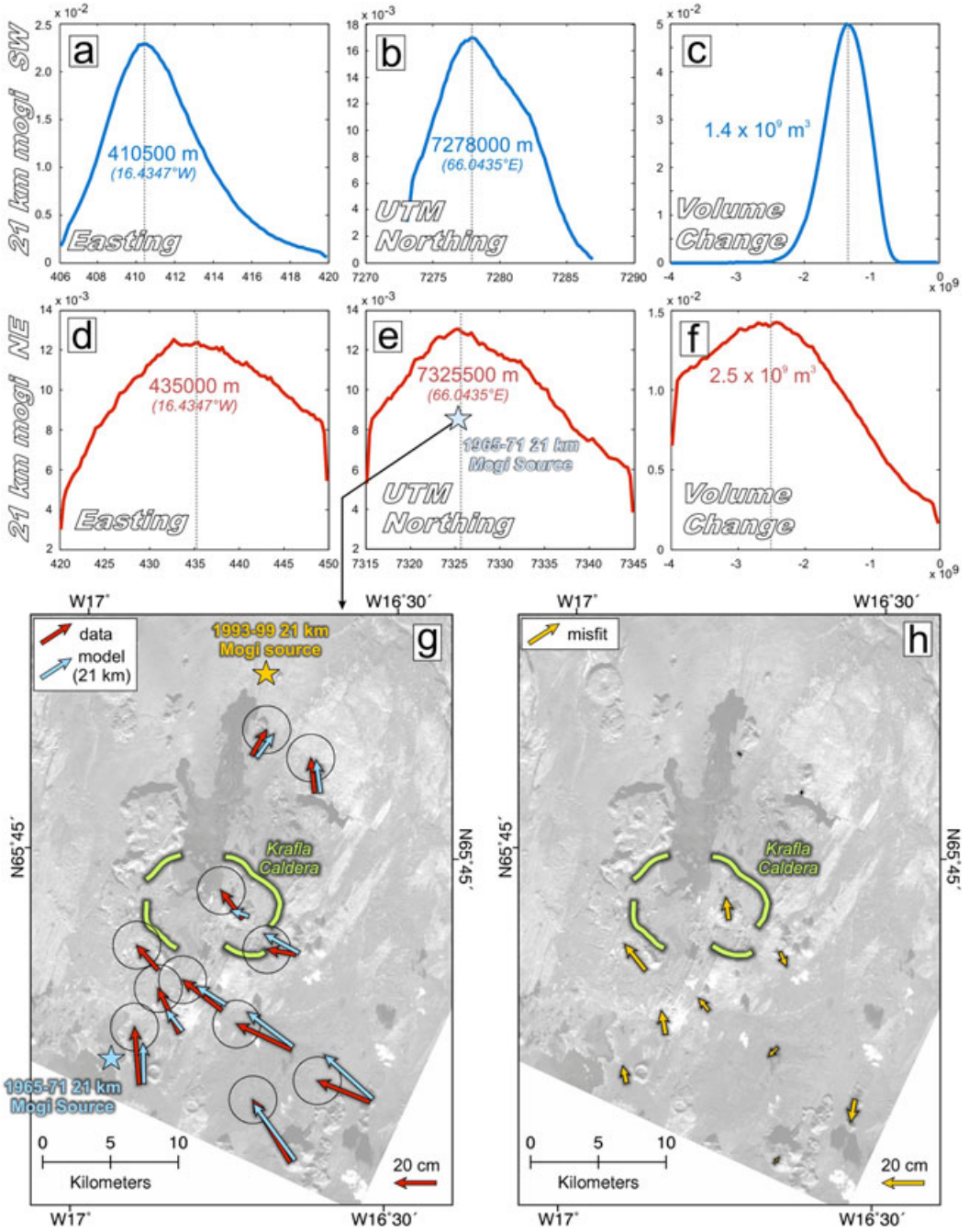

Figure 11. Probability density functions of the UTM Easting, Northing, and mogi volume change for two deflating mogi sources at 21 km depth (maximum likely depth for the crust-mantle boundary), (a–c) SW and (d–f) NE of the Krafla caldera. (g) SPOT5 satellite image of the southern Krafla rift. Displacements from triangulation data are shown by red arrows, which span the time period 1965–1971 [*Wendt et al.*, 1985]. Blue arrows show the predicted surface displacements resulting from deflation of two magma chambers at 21 depth (pale blue stars). Green lines show the extents of the caldera. Orange star shows the location of a 21 km deep magma chamber which is thought to have inflated between 1993 and 1999 [*de Zeeuw-van Dalfsen et al.*, 2004]. (h) Orange arrows show the residual displacements between the 1965 and 1971 triangulation data after removal of surface displacement produced by deflation of the two mogi sources.

[30] Although the location of the leveling line data near the dike tip may result in modeled estimates of dike opening and fault slip underrepresenting the real values for the 1978 dike injection, we can nevertheless expand on the modeling of *Rubin and Pollard* [1988] and *Rubin* [1992] by including the leveling data of *Sigurdsson* [1980], including our horizontal extension data (Figure 8d), and updating the model geometry to include

more distributed faulting on the eastern rift boundary (Figure 8e).

[31] Figures 10a–10d show the vertical and horizontal deformation profiles from *Rubin and Pollard* [1988] which best fit the leveling data. Figures 10a and 10c, and 10b and 10d show the data fit over two different length scales, one covering a 40 km profile across the rift and rift flanks and the second covering a 10 km profile across just the rift (figure inset shows the dike-fault geometry). The model fits the leveling data well, with the exception of one point on the eastern rift boundary (Figure 10c). The model also underestimates extension across the eastern rift boundary by $\sim$ 0.5 m, compared with the horizontal displacement profile from the 1976–1990 aerial photo correlation (gray profile in Figure 10d). Figures 10e–10h show similar displacement profiles calculated using an updated model geometry which includes three faults at the eastern rift boundary, thus better approximating the distributed faulting which is clearly expressed in the aerial photo correlation data (Figure 9c). In this updated dike-fault model, the surface extension (2.7 m) is around 70% of the dike opening (3.8 m), which is consistent with the values from the southern Krafla rift (section 4.1), while the dike and faults do not overlap significantly within the crust.

[32] The complicated model geometry shown in Figures 10e–10h precludes an easy exploration of all the trade-offs between the different parameters, and so it does not represent a unique solution. Nevertheless, it shows that alternative dike-fault models in which dike opening is equal to or greater than the surface extension, with only minor overlap between faults and dikes in the crust, may also explain the surface deformation data.

4.4. Deep Deflation Prior to the 1975–84 Krafla Rifting Crisis

[33] *Wendt et al.* [1985] established a triangulation network covering the southern section of the Krafla rift over the period 1965–1971 (Figure 11). The authors found contractions of $\leq$ 0.5 m across the rift zone, which they claim were not due to a scale error (the relative shortening of the lines was also confirmed by a purely directional network). Triangulation points from close to the caldera region (the "free", open circles of *Wendt et al*., 1985) also show $\sim$ 0.25 m northward motion, relative to stations in nondeforming areas further from the rift zone. The authors suggest that the northward component in these velocities is a result either from tectonic deformation prior to the rifting crisis or from rotations in the triangulation network caused by nondetected observation errors. Assuming the velocity field around the caldera is the result of magma-induced deformation, the decrease in velocities toward the caldera could be explained by deflation of a deep magma source, possibly as magma migrates to shallower depths prior to the crisis. Using a mogi source to approximate deflation of a deep magma source [e.g., *Mogi*, 1958; *de Zeeuw-van Dalfsen et al*., 2004], we invert the 1965–1971 velocity field of *Wendt et al.* [1985], using the same method as section 4.1, to determine the best-fitting parameters defining two mogi sources, location (UTM Easting and Northing) and volume change (Figure 11), to see what kind of deflation may be required to fit the triangulation data (Figures 11a–11f). Because the data NE of the caldera cannot be explained by the same mogi source which accounts for contraction south of the caldera (red arrows in Figure 11g), we invert for a second mogi source to the NE (blue star in Figure 11e shows location relative to the map in g). Because this mogi source is only constrained by two stations, the depth and location are not well constrained. Furthermore, if we allow mogi depths to vary, the inversion converges on depths of $\sim$30 km, where the deformation is unlikely to be elastic. Therefore, we fix the depth of the mogi sources to lie near the base of the crust at 21 km, consistent with seismic reflection results from the Krafla region [*Staples et al.*, 1997]. This depth is also where *de Zeeuw-van Dalfsen et al.* [2004] located an inflating mogi source for the period 1993–1999.

[34] The best-fitting mogi displacements are shown by the blue arrows in Figure 11g and the residuals in Figure 11h. Because the residuals are relatively large, the two source mogi model explored here does not represent a unique solution. The probability density functions shown in Figures 11a–11f therefore represent the most likely mogi source parameters, given the various assumptions outlined above, especially that the triangulation displacements are not the result of survey errors. The best-fitting mogi locations (blue stars in Figure 11g) lie significantly away from the caldera and the 1993–1999 mogi source, although they do generally lie along the rift axis—however, we find that the locations vary significantly depending on the mogi depths used and inclusion of the additional mogi source to the NE which is strongly influenced by only two stations. Furthermore, *Wendt et al.* [1985] state that the northward velocities may be influenced by rotations in the triangulation network caused by nondetected observation errors. Therefore, we consider our best-fitting mogi locations to be poorly constrained. Nevertheless, the volume change of the mogi source is strongly controlled by the 0.5 m of contraction across the region, which *Wendt et al.* [1985] claim is well resolved. Deflation of the southern mogi source is $\sim 1.4 \times 10^9$ m^3, while deflation of the northern source is 2.5×10^9 m^3 (although this value is also not well constrained). Therefore, the combined deflation is likely to be larger than 1.4×10^9 m^3, and potentially between 1.4 and 3.9×10^9 m^3. Nevertheless, a significant problem with modeling the triangulation data with deep deflation of mogi sources is that the volume of material that has left these deeper magma chambers must have been introduced at higher levels in the crust. This would produce a larger surface deformation signal, overprinting the deeper deflation signal, which we do not see. The question of where this material has gone is discussed in section 5.1.

5. Discussion

5.1. Summary of Deformation

[35] Using a combination of data sets, including correlation of KH9 and SPOT5 satellite images and airphotos, DEM differencing, EDM, and leveling data, we measure the deformation resulting from the 1975–1984 Krafla rift crisis. In section 4.1, we use KH9-SPOT5 correlation and EDM measurements to constrain deformation at the southern section of the rift between 1977 and 1978, and the end of the crisis. Opening occurs primarily on a 5–6 m wide dike injected between 0.5 and 5 km in the upper crust, with a surface : dike opening ratio of $\sim$ 80%. Airphoto

correlations and DEM differencing for the central section of the rift indicate that extension is partitioned onto dikes at depths of $\geq$ 1 km and normal faults at depths $\leq$ 1 km. In the northern Krafla rift, KH9-SPOT5 and airphoto correlations, DEM differencing, and leveling data indicate opening on dikes between 3 and 5 km and normal faulting at depths $\leq$ 3 km. Therefore, the upper depth limit for dikes along the Krafla rift zone varies from from 0 to 0.5 km in the south, $\sim$ 1 km in the central, and $\sim$ 2–3 km in the northern sections of the rift zone. The lower depth limit appears to be relatively consistent at 4–5 km in the southern and northern sections. Extension is partitioned onto dikes at depth and faults near the surface, and the two do not appear to overlap significantly.

[36] Based on the ratio of surface to dike opening ($\sim$ 80%), the total dike opening at depth may exceed the surface opening summarized in Figure 1b by > 20%. The total opening, averaged along the entire 70–80 km length of the rift zone is 4.3 m. Therefore, the average dike opening at depth may range between 4.3 and 5.4 m. Assuming an average vertical extent of 3–4 km for dikes injected throughout the rift, we calculate a total volume of 0.9–1.7$\times 10^9$ m^3 of magma injected into the crust over the whole crisis. The volume of the erupted material may be calculated from its aerial extent (40 km^2) and average thickness (5–10 m, determined from aerial photo DEMs), yielding 0.2–0.4 $\times$ 10^9 m^3. Therefore, the total volume of material which was erupted/injected during the Krafla rift crisis is estimated to be 1.1–2.1 $\times$ 10^9 m^3. This value is similar to the volume of material leaving the shallow magma chamber beneath the Krafla caldera between 1975 and 1984 (0.79–0.85 $\times$ 10^9 m^3) estimated by [*Harris et al.*, 2000] using geodetic data from *Tryggvason* [1984] and *Ewart et al.* [1991].

[37] Our volume estimate is also comparable with the volume change of $\geq 1.4\times 10^9$ m^3, resulting from the deflation of deep mogi sources located at 21 km depth along the Krafla rift (Figure 11). Therefore, in the 5–10 years prior to the crisis, between 1965 and 1971, magma may have migrated from the crust-mantle boundary to shallower levels in the crust. However, a major problem with this interpretation is a lack of surface deformation signal associated with a shallower inflation event for the same time period [see also *Rivalta and Segall*, 2008, for further discussion on problems associated with estimating volume changes in magma chambers]. Although *Wendt et al.* [1985] also find nearly 0.5 m of E-W extension across the Krafla caldera region between 1971 and 1975, it is not enough to account for the large volume of material leaving the deep mogi sources between 1965 and 1971. One potential way to account for the missing material once it migrated to shallower levels in the crust is by the injection of many small and diffuse dikes and sills into a mid-crust which deformed largely anelastically (Figure 12). An alternative explanation might come from the triangulation data containing scale errors across the entire network, in which case the contraction signal is simply an artifact. Nevertheless, if our mogi volume estimates are broadly correct (within an order of magnitude), the similarity of the deep deflation volumes and the total volume injected/erupted between 1975 and 84 means that the entire crust may have been activated during the rift crisis and that magma emplacement at deeper levels in the crust is also episodic. Furthermore, the crisis onset may predate the first documented dike injection in December 1975 [*Björnsson et al.*, 1977]; deep deflation and injection of diffuse dikes and sills may have begun as early as 1965, while shallower dike injection may have produced up to 0.5 m extension across the caldera region between 1971 and 1975 [*Wendt et al.*, 1985]. Nevertheless, these estimates are clearly poorly constrained, and this discussion is included simply to address the question of what may have produced a long-wavelength contraction across the caldera region between 1965 and 1971.

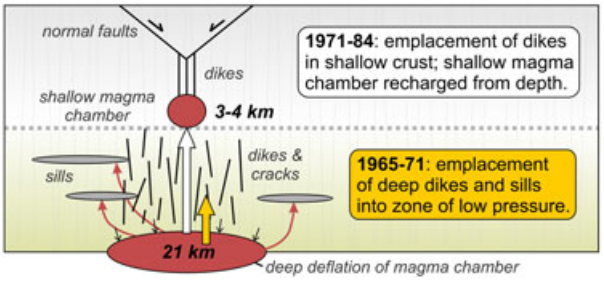

Figure 12. Cartoon showing a possible interpretation for deep magma chamber deflation and injection of diffuse dikes and sills at depth between 1965 and 1971, marking the onset of the Krafla rifting crisis. Inflation-deflation cycles of a shallow magma chamber beneath the Krafla caldera produced magma which was injected as shallow dikes and erupted at the surface between 1971 and 1984.

5.2. Partitioning of Extension Onto Dikes and Faults

[38] In contrast to the findings of *Rubin and Pollard* [1988] and *Rubin* [1992], we find a low degree of overlap between dikes and faults in the shallow crust throughout the Krafla rift, implying that fault slip is triggered by dike injection. Because the two rift-bounding faults appear to propagate upward from the upper tip of the dike, we explore a possible mechanism for triggering shallow fault slip at the surface in response to dike injection at depth [see also *Mastin and Pollard*, 1988]. Figure 13a shows the variation of horizontal (dilatational) strain resulting from a dike injection at depth, calculated using an elastic dislocation model. We use a dike opening of 3.8 m and depth extent of 2.7–5.0 km, to resemble the 1978 dike injection within the northern section of the Krafla rift (Figure 10). If normal faults localize by linkage of small-scale tensional cracks formed in the zones of maximum dilatational strain above a dike [*Agnon and Lyakhovsky*, 1995; *Pinzuti et al.*, 2010], then faults would propagate along the trajectory of maximum dilatational strain shown by the black lines in Figure 13a. The dip of this maximum strain trajectory varies with depth, steepening slightly toward the surface, with an average dip of $\sim$50°. Furthermore, the two faults are separated by a zone $\sim$ 4.3 km wide, which corresponds to the observed width of the northern Krafla rift zone (e.g., Figure 8).

[39] Immediately above the dike, the tensional (dilatational) strain exceeds the critical strain for yielding of basalt rocks (0.13–0.43 $\times$ 10^{-3}, determined by laboratory experiments of yielding for a range of intact basalts in tension, or 0.07–0.38 $\times$ 10^{-3} for semi-fractured basalts, RMR values of $\sim$75%, at low confining pressures, see *Schultz*, 1995, and

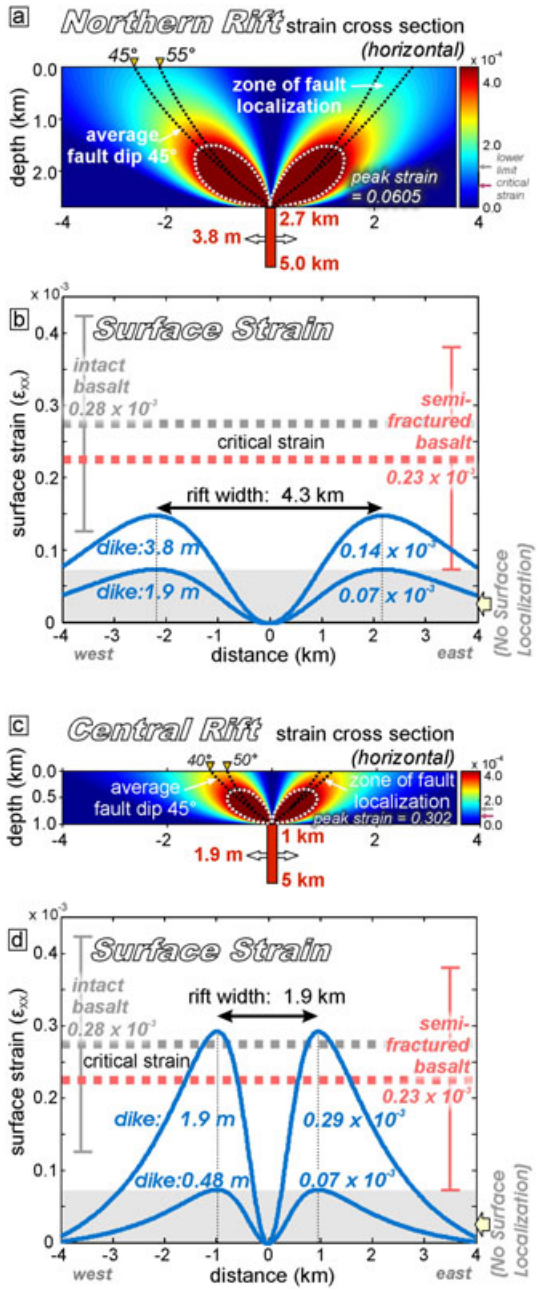

Figure 13. (a) Vertical section through the crust showing the extensional strain resulting from a dike injected between 2.7 and 5.0 km depth, and opening by 3.4 m. Black lines show the trajectory of the maximum strain above the dike, which may act as a guide for fault localization. Dotted white ellipses show the saturation limit of the color scale; the peak strain immediately above the dike reaches 0.11×10^{-3}. Pink and gray arrows highlight the lower limit of critical strain for basalt. (b) Plot showing the surface strain (blue lines) produced by the dike in Figure 13a, and a dike of 1.9 m opening. The locations of maximum surface strain are separated by a zone ~ 4.3 km wide. Critical strain for yielding determined for intact basaltic rocks is shown by gray dotted line (with error bounds), and pink dotted line for semi-fractured basalt [*Schultz*, 1995]. (c and d) Similar plots as Figures 13a and 13b, except for a 1.9 m and 0.48 m dike between 1 and 5 km depths.

references therein). Therefore, faults will localize immediately above the dike and propagate to the surface along the plane of maximum dilational strain. Thus, the width of the resulting rift zone is a function of the depth to the top of the dike injection [*Mastin and Pollard*, 1988; *Agnon and Lyakhovsky*, 1995; *Pinzuti et al.*, 2010]. Because the maximum value of dilatational strain at the surface above a 3.8 m dike injected between 2.7–5.0 km depth (0.14×10^{-3}; Figures 13a and 13b) is just above the limit for yielding of basalt at shallow depths ($0.1–0.4\times10^{-3}$), faults would be expected to propagate all the way to the surface, consistent with observations [*Sigurdsson*, 1980]. Furthermore, any dike above 1.9 m width could still potentially strain the surface rocks beyond their experimentally derived point of yielding. Nevertheless, because the maximum surface strain is also more consistent with the range of yielding values for semi-fractured basalt, our modeling approach, which treats the crust as a homogenous and purely elastic material, may be inappropriate for this setting.

[40] Figure 13c shows a similar crustal section of strain resulting from a dike between 1 and 5 km depth with normal faults above, similar to the central Krafla rift geometry (Figure 7). The average fault dip is ~ 45°, consistent with our best-fitting fault dips from elastic dislocation modeling (Figure 10), although the faults steepen toward 50° near the surface. The dike opens by 1.9 m, which is the lower limit required to activate faults at the northern end of the rift. The maximum surface strain above the dike is ~ 0.29×10^{-3} (Figure 13d), well within the region of yielding, and is higher than the equivalent surface strain for a 1.9 m dike opening (0.07×10^{-3}) at the northern end of the rift, where the dike top lies deeper within the crust (Figure 13d). Potentially, dikes of only ~ 0.5 m width at this depth range will be able to activate fault slip at the surface. Therefore, the depth to the dike top strongly controls the width of rift zone produced at the surface above the dike [as discussed previously, see *Mastin and Pollard*, 1988; *Pinzuti et al.*, 2010]. It should be noted that our estimates of the dike opening and depth extent required to produce surface faulting are likely to be correct only qualitatively, since we are comparing our results with laboratory-derived estimates on the brittle strength of basalt; our results are largely model dependent and are based on overly simple elastic dislocation models that use a vertical dislocation with constant opening; when a tapered crack model would likely be more appropriate. Nevertheless, these estimates are consistent with previous studies on fault localization above a dike [e.g., *Mastin and Pollard*, 1988; *Agnon and Lyakhovsky*, 1995; *Pinzuti et al.*, 2010].

[41] Because the 1978 dike injection extended as far as the northern end of the rift and opened by ~ 3.8 m, and presumably passed through the central section of the rift, the shallower depth of the dike top will have resulted in strong strain localization at the surface and slip on faults. However, up to 2 m of fault slip was also observed at the northern end of the rift at the onset of the crisis in 1976 yet did not appear to activate surface faults in the central section of the rift [*Hollingsworth et al.*, 2012]. If the shallower depth of diking in the central rift leads to more localized surface strain during dike injection, the lack of fault slip in 1976 implies that the rocks may be relatively stronger in the central Krafla rift (or weaker in the northern rift). An alternative, and more likely explanation given the probable uniform rock

type throughout the rift, may come from a weakening mechanism introduced as the dike passes along the rift when the pressure in the dike tip cavity is no longer maintained by magmatic volatiles [*Ziv et al.*, 2000]. Another possibility is that a stronger extensional stress at the northern end of the rift, compared with the central rift, may have caused magma to preferentially accumulate in the north, thereby passing through the central rift section without accumulating there; although this hypothesis requires that the magma does not freeze while passing through the central rift section. The dike could also have passed through the central rift at greater depths than at the northern end of the rift, thereby only activating faults in the north. However, these hypotheses require an explanation either for the dike increasing and then decreasing in depth as it propagates along the rift, or the northern rift being in a significantly increased state of tensional stress than the central rift.

[42] Our best-fitting fault dips from elastic dislocation modeling of both the central and northern sections of the Krafla rift range between 40–50°. Although we do not fully explore the range of fault dips using an inversion approach, we generally find that steeper fault dips do not produce enough horizontal extension to match the aerial photo and KH9-SPOT5 correlation data. Although these angles are less than the theoretical 60° for normal fault initiation, as predicted by Mohr-Coulomb faulting theory, they are consistent with the average dip of normal faulting earthquakes from oceanic spreading centers [*Thatcher and Hill*, 1995]. Possible explanations for these lower angles may include reactivation of 45° normal faults formed above dike injections as new oceanic crust is created, and relatively low coefficients of friction within spreading centers. Therefore, as oceanic crust migrates away from spreading centers with time, through repeated dike injection, a pervasive structural weakness is produced (oriented ∼45°), which is exploited in future earthquakes [e.g. *Thatcher and Hill*, 1995]. Nevertheless, for large strains, the theories of rigid-plasticity and elasto-plasticity both predict normal fault dips of 45–50° above a vertical dike [*Gerbault et al.*, 1998].

5.3. Contribution of Aseismic and Seismic Deformation

[43] The only significant earthquake of the Krafla crisis occurred at the northern end of the rift on 13 January 1976 (M_w 6.3; see Figure 1c). Although the depth of this earthquake is not well constrained by the NEIC and Global CMT catalogs, the depths of post-1990 microearthquakes surrounding the 1976 epicenter [*Einarsson*, 1991; *Rögnvaldsson et al.*, 1998] range from from 3 to 15 km [as detected by the South Iceland Lowland (SIL) seismic network; see also *Hollingsworth et al*., 2012], therefore suggesting a similar depth for the 1976 event. Studies of the microseismicity for the wider Tjörnes Fracture Zone region show similar earthquake depths, with the majority of events occurring between 3 and 8 km depth [*Rögnvaldsson et al.*, 1998]. *Hollingsworth et al.* [2012] suggest the CLVD component of the 1976 focal mechanism (Figure 1c) may result from a volumetric change associated with dike injection beneath the northern section of the rift. Provided the dike opened by more than ∼3.5 m, and at depths greater than or equal to 3 km, normal faults would be expected to localize above the dike, reaching the surface in a 5–6 km wide rift zone. This value is consistent with field and geodetic measurements of surface deformation covering the early stages of the Krafla crisis, which indicate slip on normal faults in the Jökulsá á Fjöllum river delta (Figure 1c), separated by a 5–6 km wide zone of subsidence [*Tryggvason*, 1976; *Hollingsworth et al.*, 2012].

[44] The seismic moment released by the 1976 earthquake was 3.3×10^{18} Nm (Global CMT catalog). Additional earthquakes recorded by the NEIC catalog during the crisis (between 20th December 1975 and 1st October 1984) adds an additional 2.5×10^{18} Nm (from earthquakes located within 10 km of the 80 km long rift zone). Therefore, the total seismic moment released during the crisis is $\sim5.8\times10^{18}$ Nm, which is equivalent to one M_w 6.7 earthquake. The total geodetic moment for a dike measuring 70–80 km by 3–4 km, and opening by 4.3–5.4 m, is $2.7–5.2\times10^{19}$ Nm (assuming a rigidity modulus of 30 GPa). The moment release from two faults 70–80 km long, 1–2 km wide, and slipping ∼4 m is $1.7–3.8\times10^{19}$ Nm. Therefore, the combined geodetic moment release from both dike injection and fault slip is $4.4–9.0\times10^{19}$ Nm, equivalent to one M_w 7.0–7.2 earthquake. The seismic moment therefore only accounts for ∼9% of the total geodetic moment. Similar values of 8% were obtained for the 1978 Asal rift crisis [*Stein et al.*, 1991], and 10% for the 2005 dike injection which kick-started the 2005–2009 Afar crisis [*Grandin et al.*, 2009].

5.4. Schematic Model of the Krafla Crisis and Longer-Term Rifting

[45] Figure 14a shows a cartoon illustration of the possible structure of the Krafla rift zone, based on the findings of this paper. Beneath the Krafla caldera, the high geothermal gradient results in a shallow brittle-ductile transition (BDT; Figure 14b) [see also *Grandin et al*., 2012]. Dikes are injected in the depth range where the magma pressure exceeds the horizontal/tectonic stress (σ_3). As the dike propagates along the rift, the decreasing geothermal gradient causes the BDT to increase in depth (Figure 14c). As the BDT depth increases, so too does the difference between the tectonic stress (σ_3) and lithostatic stress (σ_1), thus causing the base of the propagating dike to increase in depth. Furthermore, with continued dike propagation, the magma pressure (ρ_m) decreases as magma is removed from the chamber, forcing the top of the dike to increase in depth (Figure 14d). These two effects work in tandem, thereby resulting in the gradual deepening of laterally propagating dikes away from the magma chamber. Evidence for this effect can be seen at the surface, as the width of the Krafla rift zone increases away from the caldera region (Figure 1c). This hypothesis assumes minor overlap between dikes and faults.

[46] Topography is also thought to control the geometry of diking and faulting in rift zones over geological timescales [*Behn et al.*, 2006]. As dikes propagate to greater depths with distance from the magma chamber, the normal faults above them become correspondingly larger. This creates greater rift flank topography which leads to flexural compression in the base of the crust beneath the rift, thus forcing dikes closer to the surface [*Behn et al.*, 2006]. Shallow dikes produce smaller faults, which reduce the creation of rift flank topography. Therefore, over geologic timescales, lateral dike injection appears to be a self-limiting process whereby dike-generated faulting and topography result in an efficient feedback mechanism that controls the

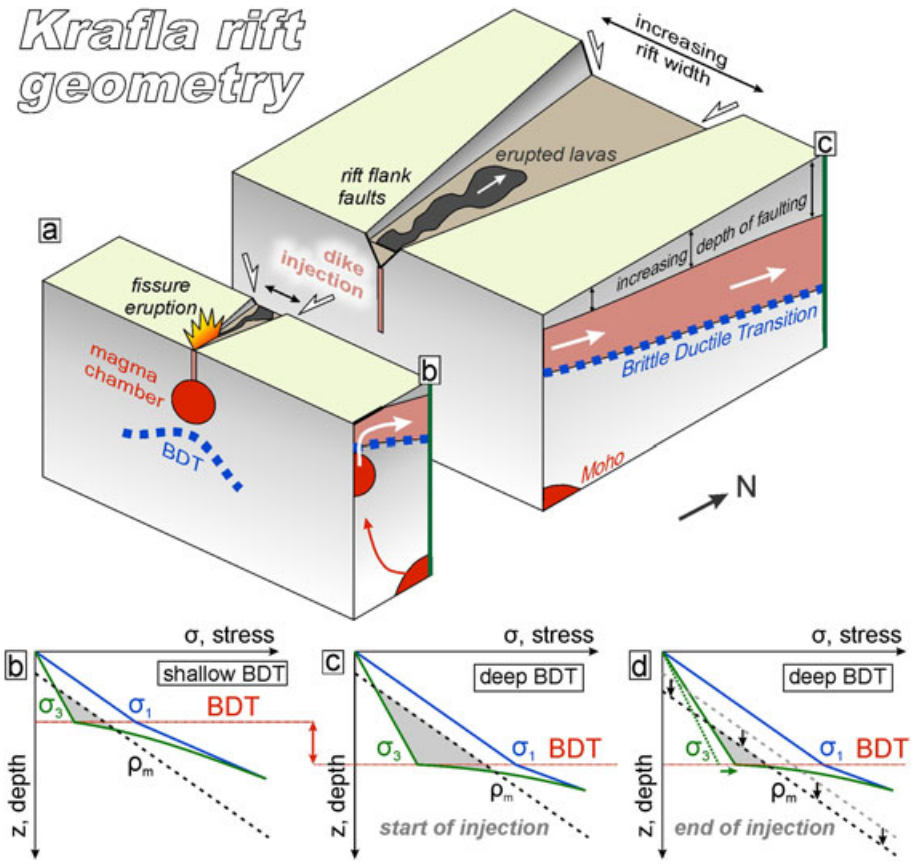

Figure 14. (a) Cartoon perspective image summarizing the main features of the Krafla rift zone. The high geothermal gradient beneath the Krafla caldera results in a relatively shallow brittle-ductile transition (BDT). As the dikes propagate away from the magma chamber, the geothermal gradient decreases resulting in a deepening BDT. As dikes propagate to greater depths, the normal faults which localize above them produce a progressively widening rift zone at the surface. The depth to the top of the propagating dike probably also increases, as magma migrates into more tensile, deeper parts of the crust. These concepts may also be illustrated by plots showing the variation of crustal stress with depth. (b) Above the magma chamber, dikes are injected in the crust where the magma pressure (ρ_m, dashed black line) exceeds the tectonic (extensional) stress (σ_3, solid green line), i.e., the gray area beneath the dashed black line. (c) As the BDT increases in depth, so too does the zone in which a pressurized magma can inject (gray region). (d) As magma is drawn out of the chamber, the magma pressure decreases, causing the top of the dike to increase in depth.

time-averaged distribution of magma accretion within the crust [*Behn et al*., 2006].

6. Conclusions

[47] Correlation of KH9 spy and SPOT5 satellite images, airphotos, DEM differencing, EDM, and leveling survey data is used to constrain the deformation resulting from the 1975–1984 Krafla rifting crisis. Due to the different spatial and temporal coverage of the different data sets, we examine deformation in the southern, central, and northern sections of the rift separately. We find that diking typically extends to depths of ~5 km, while the top of the dike increases from 0 km in the caldera region (where lava was erupted at the surface) to ~3 km at the northern end of the rift. Extension is accommodated by diking at depth, and normal faulting in the shallowest crust. Immediately above a dike injection, rocks are strained beyond their critical limit for yielding, thereby causing faults to form and propagate toward the surface along the trajectory of maximum dilatational strain. This model assumes that faults form by the linkage of small vertical cracks which may preferentially form in the zones of maximum dilatational strain. Therefore, faults appear to form passively in response to diking at depth, with minor moment release at seismic frequencies. Because faulting relieves tension in the shallowest parts of the crust, relatively fewer dikes will be injected in this zone. This is consistent with the relatively sparse record of erupted lavas covering the northern section of the rift, compared with the caldera region in the south (the northern rift is predominantly covered by post-glacial lavas erupted ~10 kybp) [*Saemundsson*, 1991; *Dauteuil et al*., 2001; *Slater et al*., 2001; *Saemundsson et al*., 2012].

[48] In the southern section of the Krafla rift, we find surface opening to be ~80% of the dike opening at depth; therefore, over the 70–80 km length of the rift, the average surface opening of 4.3 m may give rise to 5.4 m

for the average total dike opening. Combining these estimates with our estimated depth range for diking (3–4 km), we calculate the geodetic moment released over the entire Krafla crisis, $4.4–9.0\times10^{19}$ Nm, which is an order of magnitude higher than the seismic moment released over the same time period, $\sim5.8\times10^{18}$ Nm. The total volume of magma added to the Krafla upper crust throughout the crisis was $1.1–2.1\times10^{9}$ m^3 (i.e., the sum of both intruded and erupted material). This value is remarkably similar to the volume of magma, $\geq1.4\times10^{9}$ m^3, which may have migrated from 21 km to shallower depths beneath the caldera region between 1965–71, prior to the onset of the crisis in 1975. However, because there is no corresponding signal for inflation of a shallow magma chamber between 1965 and 1971, the pre-rift contraction may simply reflect an error in the 1965–71 triangulation survey (thus, it is simply coincidental that the two volumes are similar in magnitude). However, if diffuse diking and sill injection at deep-to-middle crust depths occurred, with minimal surface signal, then it suggests that the Krafla rift crisis may have begun as early as 1965, with the onset of deep magma movements before gradually migrating to shallower depths. If this behavior typically precedes all such rifting crises, it suggests that future events may potentially be forecast from the detection of deep magma movements in the years preceding a crisis.

[49] This study highlights how optical image correlation using inexpensive declassified spy satellite and aerial photography can provide important constraints on the deformation field resulting from past earthquake and volcanic events.

[50] **Acknowledgments.** Part of this research was funded by the Gordon and Betty Moore Foundation through Grant GBM 2808 to the Advanced Earth Observation Project at Caltech. We also thank the Keck Institute for Space Studies for financial support. Thora Arnadottir kindly provided EDM displacement data for the Krafla rift from 1978 to 1989 [*Tryggvason*, 1991]. Arzan Surazakov provided helpful advice and discussion regarding ortho-rectification of KH9 Hexagon data. The decision to look at displacement in the epipolar perpendicular direction was inspired by discussions with Renaud Binet. Bjarney Gudbjornsdottir and Carsten Kristinsson (National Land Survey of Iceland) were extremely helpful with locating and scanning all airphotos used in this study. Tim Smith (USGS contractor working within Earth Resources Observation and Science, EROS) provided valuable assistance with scanning KH9 spy satellite images. This work greatly benefited from detailed reviews by Tim Wright and an anonymous reviewer. Various aspects of this study benefited from discussions with Raphael Grandin, Mark Simons, Sylvain Barbot, John Maclennan, Dan McKenzie, Gilles Peltzer, and Alex Copley. We are grateful to Heather Steele and Lisa Christiansen, who helped with ordering imagery and provided GIS support. Various images in this paper were created using the public domain Generic Mapping Tools (GMT) software [*Wessel and Smith*, 1998]. This is Tectonics Observatory contribution number 232.

References

Abdallah, A., V. Courtillot, M. Kasser, A. Le Dain, J. Léipine, B. Robineau, J. Ruegg, P. Tapponnier, and A. Tarantola (1979), Relevance of Afar seismicity and volcanism to the mechanics of accreting plate boundaries, *Nature*, *282*, 17–23.

Agnon, A., and V. Lyakhovsky (1995), Damage distribution and localization during dyke intrusion, in *Physics and Chemistry of Dykes*, edited by H. Baer, pp. 65–78, Balkema, Rotterdam, Netherlands.

Anderson, K., and P. Segall (2013), Bayesian inversion of data from effusive volcanic eruptions using physics-based models: Application to Mount St. Helens 2004–2008, *J. Geophys. Res. Solid Earth*, doi:10.1002/jgrb.50169.

Árnadóttir, T., F. Sigmundsson, and P. Delaney (1998), Sources of crustal deformation associated with the Krafla, Iceland, eruption of September 1984, *Geophys. Res. Lett.*, *25*(7), 1043–1046.

Árnadóttir, T., B. Lund, W. Jiang, H. Geirsson, H. Björnsson, P. Einarsson, and T. Sigurdsson (2009), Glacial rebound and plate spreading: Results from the first countrywide GPS observations in Iceland, *Geophys. J. Int.*, *177*, 691–716, doi:10.1111/j.1365-246X.2008.04059.x.

Ayoub, F., S. Leprince, and J. Avouac (2009a), Co-registration and correlation of aerial photographs for ground deformation measurements, *ISPRS J. Photogramm. Remote Sens.*, *64*(6), 551–560.

Ayoub, F., S. Leprince, and L. Keene (2009b), *COSI-CORR User's Guide. Co-registration of Optically Sensed Images and Correlation*, Calif. Inst. of Technol., Pasadena, Calif.

Barisin, I., S. Leprince, B. Parsons, and T. Wright (2009), Surface displacements in the September 2005 Afar rifting event from satellite image matching: Asymmetric uplift and faulting, *Geophys. Res. Lett.*, *36*, L07301, doi:10.1029/2008GL036431.

Behn, M., and G. Ito (2008), Magmatic and tectonic extension at mid-ocean ridges: 1. Controls on fault characteristics, *Geochem. Geophys. Geosyst.*, *9*, Q08O10, doi:10.1029/2008GC001965.

Behn, M., W. Buck, and I. Sacks (2006), Topographic controls on dike injection in volcanic rift zones, *Earth Planet. Sci. Lett.*, *246*(3–4), 188–196, doi:10.1016/j.epsl.2006.04.005.

Björnsson, A., K. Saemundsson, P. Einarsson, E. Tryggvason, and K. Gronvold (1977), Current rifting episode in North Iceland, *Nature*, *266*, 318–323.

Brandsdotttir, B., W. Menke, P. Einarsson, R. White, and R. Staples (1997), Faroe-Iceland ridge experiment 2. Crustal structure of Krafia central volcano, *J. Geophys. Res.*, *102*, 7867–7886.

Buades, A., B. Coll, and J. Morel (2006), The staircasing effect in neighborhood filters and its solution, *IEEE Trans. Image Process.*, *15*(6), 1499–1505.

Buck, W., L. Lavier, and A. Poliakov (2005), Modes of faulting at mid-ocean ridges, *Nature*, *434*, 719–723.

Buck, W., P. Einarsson, and B. Brandsdóttir (2006), Tectonic stress and magma chamber size as controls on dike propagation: Constraints from the 1975–1984 Krafla rifting episode, *J. Geophys. Res.*, *111*, B12404, doi:10.1029/2005JB003879.

Dauteuil, O., J. Angelier, F. Bergerat, S. Verrier, and T. Villemin (2001), Deformation partitioning inside a fissure swarm of the northern Icelandic rift, *J. Struct. Geol.*, *23*, 1359–1372.

De Chabalier, J., and J. Avouac (1994), Kinematics of the Asal rift (Djibouti) determined from the deformation of Fieale volcano, *Science*, *265*, 1677–1681.

de Zeeuw-van Dalfsen, E., R. Pedersen, F. Sigmundsson, and C. Pagli (2004), Satellite radar interferometry 1993–1999 suggests deep accumulation of magma near the crust-mantle boundary at the Krafla volcanic system, Iceland, *Geophys. Res. Lett.*, *31*, L13611, doi:10.1029/2004GL020059.

Einarsson, P. (1991), Earthquakes and present-day tectonism in Iceland, *Tectonophysics*, *189*, 261–279.

Elliott, J., E. Nissen, P. England, J. Jackson, S. Lamb, Z. Li, M. Oehlers, and B. Parsons (2012), Slip in the 2010–2011 Canterbury earthquakes, New Zealand, *J. Geophys. Res.*, *117*, B03401, doi:10.1029/2011JB008868.

Ewart, J., B. Voight, and A. Björnsson (1991), Elastic deformation models of Krafla Volcano, Iceland, for the decade 1975 through 1985, *Bull. Volcanol.*, *53*, 436–459.

Fialko, Y., D. Sandwell, M. Simons, and P. Rosen (2005), Three-dimensional deformation caused by the Bam, Iran, earthquake and the origin of shallow slip deficit, *Nature*, *435*, 295–299, doi:10.1038/nature03425.

Gerbault, M., A. Poliakov, and M. Daignieres (1998), Prediction of faulting from the theories of elasticity and plasticity: What are the limits? *J. Struct. Geol.*, *20*(2–3), 301–320.

Goossens, B., H. Luong, A. Pizurica, and W. Philips (2008), An improved non-local denoising algorithm, in *Proceedings of the 2008 International Workshop on Local and Non-Local Approximation in Image Processing*, edited by J. Astola, K. Egiazarian, and V. Katkovnik, pp. 143–156, Lausanne, Switzerland.

Grandin, R., A. Socquet, M.-P. Doin, E. Jacques, J.-B. de Chabalier, and G. King (2010), Transient rift opening in response to multiple dike injections in the Manda Hararo rift (Afar, Ethiopia) imaged by time-dependent elastic inversion of interferometric synthetic aperture radar data, *J. Geophys. Res.*, *115*, B09403, doi:10.1029/2009JB006883.

Grandin, R., A. Socquet, C. Doubre, E. Jacques, and G. King (2012), Elastic thickness control of lateral dyke intrusion at mid-ocean ridges, *Earth Planet. Sci. Lett.*, *319–320*, 83–95.

Grandin, R., et al. (2009), September 2005 Manda Hararo-Dabbahu rifting event, Afar (Ethiopia): Constraints provided by geodetic data, *J. Geophys. Res.*, *114*, B08404, doi:10.1029/2008JB005843.

Hamling, I., A. Ayele, L. Bennati, E. Calais, C. Ebinger, D. Keir, E. Lewi, T. Wright, and G. Yirgu (2009), Geodetic observations of the ongoing

Dabbahu rifting episode: New dyke intrusions in 2006 and 2007, *Geophys. J. Int.*, *178*, 989–1003.

Hamling, I., T. Wright, E. Calais, L. Bennati, and E. Lewi (2010), Stress transfer between thirteen successive dyke intrusions in Ethiopia, *Nat. Geosci.*, *3*, 713–717.

Harris, A., J. Murray, S. Aries, M. Davies, L. Flynn, M. Wooster, R. Wright, and D. Rothery (2000), Effusion rate trends at Etna and Krafla and their implications for eruptive mechanisms, *J. Volcanol. Geotherm. Res.*, *102*, 237–270.

Hollingsworth, J., S. Leprince, F. Ayoub, and J. Avouac (2012), Deformation during the 1975–1984 Krafla rifting crisis, NE Iceland, measured from historical optical imagery, *J. Geophys. Res., 117*, B11407, doi:10.1029/2012JB009140.

Ito, G., and M. Behn (2008), Magmatic and tectonic extension at mid-ocean ridges: 2. Origin of axial morphology, *Geochem. Geophys. Geosyst.*, *9*, Q09O12, doi:10.1029/2008GC001970.

Leprince, S., F. Ayoub, Y. Klinger, and J.-P. Avouac (2007a), Co-registration of optically sensed images and correlation (COSI-Corr): An operational methodology for ground deformation measurements, in *International Geoscience and Remote Sensing Symposium (IGARSS),* vol. 6, pp. 2700–2702, IEEE International, Barcelona, Spain.

Leprince, S., S. Barbot, F. Ayoub, and J.-P. Avouac (2007b), Orthorectification, coregistration, and subpixel correlation of satellite images, application to ground deformation measurements, *IEEE Trans. Geosci. Remote Sens.*, *45*(6), 1529–1558.

Leprince, S., E. Berthier, F. Ayoub, C. Delacourt, and J. Avouac (2008), Monitoring earth surface dynamics with optical imagery, *Eos Trans. AGU*, *89*(1), 1–2.

Manighetti, I., M. Campillo, C. Sammis, M. Mai, and G. King (2005), Evidence for self-similar, triangular slip distributions on earthquakes: Implications on earthquake and fault mechanics, *J. Geophys. Res.*, *110*, B05302, doi:10.1029/2004JB003174.

Mastin, L., and D. Pollard (1988), Surface deformation and shallow dike intrusion processes at Inyo Craters, Long Valley, California, *J. Geophys. Res.*, *93*(B11), 13,221–13,235.

Mogi, K. (1958), Relations between the eruptions of various volcanoes and the deformation of the ground surface around them, *Bull. Earthquake Res. Inst.*, *36*, 99–134.

Ofeigsson, B., A. Hooper, F. Sigmundsson, E. Sturkell, and R. Grapenthin (2011), Deep magma storage at Hekla volcano, Iceland, revealed by InSAR time series analysis, *J. Geophys. Res.*, *116*, B05401, doi:10.1029/2010JB007576.

Okada, Y. (1985), Surface deformations due to shear and tensile faults in a half-space, *Bull. Seismol. Soc. Am.*, *75*, 1135–1154.

Okada, Y. (1992), Internal deformation due to shear and tensile faults in a half-space, *Bull. Seismol. Soc. Am.*, *82*(2), 1018–1040.

Pinzuti, P., A. Mignan, and G. King (2010), Surface morphology of active normal faults in hard rock: Implications for the mechanics of the Asal Rift, Djibouti, *Earth Planet. Sci. Lett.*, *299*, 169–179.

Rivalta, E., and P. Segall (2008), Magma compressibility and the missing source for some dike intrusions, *Geophys. Res. Lett.*, *35*, L04306, doi:10.1029/2007GL032521.

Rögnvaldsson, S., A. Gudmundsson, and R. Slunga (1998), Seismotectonic analysis of the Tjörnes Fracture Zone, an active transform fault in north Iceland, *J. Geophys. Res.*, *103*(B12), 30,117–30,129.

Rubin, A. (1992), Dike-induced faulting and graben subsidence in volcanic rift zones, *J. Geophys. Res.*, *97*(B2), 1839–1858.

Rubin, A., and D. Pollard (1988), Dike-induced faulting in rift zones of Iceland and Afar, *Geology*, *16*, 413–417.

Saemundsson, K. (1991), *Náttúra aslands*, pp. 25–95, Jardfraedi Kroflukerfisins [The Geology of the Krafla volcanic System], Hid aslenska Natturufraedifelag, Reykjavik, Iceland.

Saemundsson, K., A. Hjartarson, I. Kaldal, M. Sigurgeirsson, S. Kristinsson, and S. Víkingsson (2012), Geological Map of the Northern Volcanic Zone, Iceland. Nothern Part 1:100 000, *Iceland GeoSurvey and Landsvirkjun*, Reykjavik, Iceland.

Schultz, R. (1995), Limits on strength and deformation properties of jointed basaltic rock masses, *Rock Mech. Rock Eng.*, *28*(1), 1–15.

Sigmundsson, F. (2006), *Iceland Geodynamics: Crustal Deformation and Divergent Plate Tectonics*, 209 pp., Springer, Chichester, U. K.

Sigurdsson, O. (1980), Surface deformation of the Krafla fissure swarm in two rifting events, *J. Geophys.*, *47*, 154–159.

Simons, M., Y. Fialko, and L. Rivera (2002), Coseismic deformation from the 1999 Mw 7.1 Hector Mine, California, earthquake as inferred from InSAR and GPS observations, *Bull. Seismol. Soc. Am.*, *92*, 1390–1402.

Slater, L., D. McKeznie, K. Grönvold, and N. Shimizu (2001), Melt generation and movement beneath Theistareykir, NE Iceland, *J. Petrol.*, *42*(2), 321–354, doi:10.1093/petrology/42.2.321.

Staples, R., R. White, B. Brandsdotttir, W. Menke, P. Maguire, and J. McBride (1997), Färoe-Iceland Ridge Experiment 1. Crustal structure of northeastern Iceland, *J. Geophys. Res.*, *102*(B4), 7849–7866.

Stein, R., P. Briole, J. Ruegg, P. Tapponnier, and F. Gasse (1991), Contemporary, Holocene, and Quaternary deformation of the Asal Rift, Djibouti: Implications for the mechanics of slow spreading ridges, *J. Geophys. Res.*, *96*(B13), 21,789–21,806.

Sudhaus, H., and S. Jónsson (2011), Source model for the 1997 Zirkuh earthquake (Mw = 7.2) in Iran derived from JERS and ERS InSAR observations, *Geophys. J. Int.*, *185*, 676–692.

Tarantola, A. (2004), *Inverse Problem Theory and Methods for Model Parameter Estimation,* 1st ed., SIAM: Society for Industrial and Applied Mathematics, Philadelphia, Pa.

Thatcher, W., and D. Hill (1995), A simple model for the fault-generated morphology of slow-spreading mid-ocean ridges, *J. Geophys. Res.*, *100*, 561–570.

Tryggvason, E. (1976), Ground movement in North Iceland during the earthquake swarm of 1975-1976 (in Icelandic, with English summary), *Náttúrufraedingurinn*, *46*, 124–128.

Tryggvason, E. (1984), Widening of the Krafla fissure swarm during the 1975–1981 volcano-tectonic episode, *Bull. Volcanol.*, *47*(1), 47–69.

Tryggvason, E. (1991), Magnitude of deformation of active volcanoes in Iceland, *Cahiers du Centre européen de géodynamique et de séismologie*, *4*, 37–49.

Tryggvason, E. (1994), Surface deformation at the Krafla volcano, North Iceland, 1982–1992, *Bull. Volcanol.*, *2*, 98–107, doi:10.1007/BF00304105.

Wendt, K., D. Möller, and B. Ritter (1985), Geodetic measurements of surface deformations during the present rifting episode in NE Iceland, *J. Geophys. Res.*, *90*(B12), 10,163–10,172, doi:10.1029/jb090ib12p10163.

Wessel, P., and W. H. F. Smith (1998), New, improved version of generic mapping tools released, *Eos Trans. AGU*, *79*(47), 579.

Wolf, P., B. DeWitt, and B. Wilkinson (2000), *Elements of Photogrammetry With Application in GIS,* 608 pp. 3rd ed., McGraw-Hill, New York.

Wright, T., C. Ebinger, J. Biggs, A. Ayele, G. Yirgu, D. Keir, and A. Stork (2006), Magma-maintained rift segmentation at continental rupture in the 2005 Afar dyking episode, *Nature*, *442*, 291–294.

Wright, T. et al. (2012), Geophysical constraints on the dynamics of spreading centres from rifting episodes on land, *Nat. Geosci.*, *5*, 242–250.

Ziv, A., A. Rubin, and A. Agnon (2000), Stability of dike intrusion along preexisting fractures, *J. Geophys. Res.*, *105*, 5947–5961.